

NAVAL POSTGRADUATE SCHOOL



DISSERTATION

FREE ELECTRON LASER DEVELOPMENT FOR DIRECTED ENERGY

by

Roger D. McGinnis

December 2000

Dissertation Supervisor:

William B. Colson

Approved for public release; distribution is unlimited.

20010328 055

REPORT DOCUMENTATION PAGE			Form Approved OMB No. 0704-0188	
Public reporting burden for this collection of information is estimated to average 1 hour per response, including the time for reviewing instruction, searching existing data sources, gathering and maintaining the data needed, and completing and reviewing the collection of information. Send comments regarding this burden estimate or any other aspect of this collection of information, including suggestions for reducing this burden, to Washington headquarters Services, Directorate for Information Operations and Reports, 1215 Jefferson Davis Highway, Suite 1204, Arlington, VA 22202-4302, and to the Office of Management and Budget, Paperwork Reduction Project (0704-0188) Washington DC 20503.				
1. AGENCY USE ONLY (Leave blank)		2. REPORT DATE December 2000		3. REPORT TYPE AND DATES COVERED Doctoral Dissertation
4. TITLE AND SUBTITLE Free Electron Laser Development For Directed Energy			5. FUNDING NUMBERS	
6. AUTHOR(S) McGinnis, Roger D.				
7. PERFORMING ORGANIZATION NAME(S) AND ADDRESS(ES) Naval Postgraduate School Monterey, CA 93943-5000			8. PERFORMING ORGANIZATION REPORT NUMBER	
9. SPONSORING / MONITORING AGENCY NAME(S) AND ADDRESS(ES)			10. SPONSORING / MONITORING AGENCY REPORT NUMBER	
11. SUPPLEMENTARY NOTES The views expressed in this thesis are those of the authors and do not reflect the official policy or position of the Department of Defense or the U.S. Government.				
12a. DISTRIBUTION / AVAILABILITY STATEMENT Approved for public release; distribution is unlimited.			12b. DISTRIBUTION CODE	
13. ABSTRACT This dissertation investigates power requirements for a Free Electron Laser to burn through various missile radome materials. It also includes computer simulation results for several FEL system configurations designed to achieve maximum power while maintaining strict energy spread constraints. The method used to determine power requirements to burn through materials was to use the Thomas Jefferson National Accelerator Facility's Free Electron Laser to conduct material damage experiments. As the laser was improved and increased in power, the laser spot sizes on the target materials was increased while maintaining a constant irradiance. The key results from these experiments included determining minimal spot sizes that can be used for future experiments, and validation that an irradiance level of 10 kW/cm ² can burn through most missile radome materials in a few seconds. The computer simulations involved changing various parameters of a FEL such as electron energy levels, pulse lengths, magnetic field strengths, desynchronism, as well as several other parameters, to determine the best possible configuration to achieve the desire power levels and energy spread requirements for development of a weapon size FEL. The results indicate that for the proposed designs, both the required power and the required energy spread limit can be met.				
14. SUBJECT TERMS Free Electron Laser, Laser Damage, Anti-Ship Cruise Missiles			15. NUMBER OF PAGES 149	
			16. PRICE CODE	
17. SECURITY CLASSIFICATION OF REPORT Unclassified	18. SECURITY CLASSIFICATION OF THIS PAGE Unclassified	19. SECURITY CLASSIFICATION OF ABSTRACT Unclassified	20. LIMITATION OF ABSTRACT UL	

THIS PAGE INTENTIONALLY LEFT BLANK

Approved for public release; distribution is unlimited.

FREE ELECTRON LASER DEVELOPMENT FOR DIRECTED ENERGY

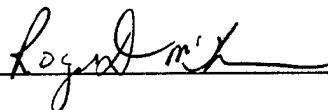
Roger D. McGinnis
Commander, United States Navy
B.S., Georgia Institute of Technology, 1982
M.S., Naval Postgraduate School, 1994

Submitted in partial fulfillment of the
requirements for the degree of

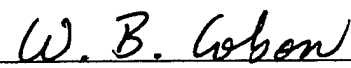
DOCTOR OF PHILOSOPHY IN PHYSICS


from the

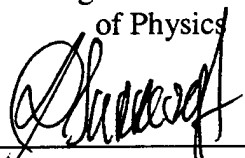
NAVAL POSTGRADUATE SCHOOL
December 2000

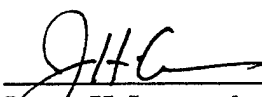
Author: 

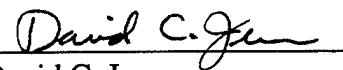
Approved by:

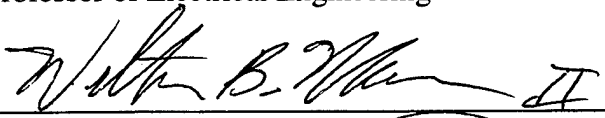

William B. Colson
Distinguished Professor
of Physics

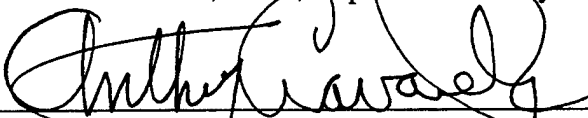

Robert L. Armstead
Professor of Physics


Andres Larraza
Professor of Physics


James H. Luscombe
Professor of Physics


David C. Jenn
Professor of Electrical Engineering

Approved by: 
William B. Maier, Chair, Department of Physics

Approved by: 
Anthony Ciavarella, Associate Provost for Instruction

THIS PAGE INTENTIONALLY LEFT BLANK

ABSTRACT

This dissertation investigates power requirements for a Free Electron Laser to burn through various missile radome materials. It also includes computer simulation results for several FEL system configurations designed to achieve maximum power while maintaining strict energy spread constraints.

The method used to determine power requirements to burn through materials was to use the Thomas Jefferson National Accelerator Facility's Free Electron Laser to conduct material damage experiments. As the laser was improved and increased in power, the laser spot sizes on the target materials were increased while maintaining a constant irradiance. The key results from these experiments included determining minimal spot sizes that can be used for future experiments, and validation that an irradiance level of 10 kW/cm^2 can burn through most missile radome materials in a few seconds.

The computer simulations involved changing various parameters of a FEL such as electron energy levels, pulse lengths, magnetic field strengths, desynchronism, as well as several other parameters, to determine the best possible configuration to achieve the desired power levels and energy spread requirements for development of a megawatt size FEL. The results indicate that for the proposed designs, both the required power and the required energy spread limit can be met.

THIS PAGE INTENTIONALLY LEFT BLANK

TABLE OF CONTENTS

I.	INTRODUCTION.....	1
II.	MATERIAL DAMAGE EXPERIMENTS.....	7
A.	THEORY.....	7
1.	Required Power to Destroy Target.....	9
2.	Scaling Laws and Minimal Spot Size.....	13
3.	Pulse Train.....	15
B.	MATERIALS USED IN EXPERIMENTS.....	16
1.	Thermal Diffusion Calculations.....	17
2.	Experimental Results.....	19
C.	CONCLUSIONS.....	32
1.	Approximation Methods.....	33
2.	Scaling.....	34
3.	FEL Pulse Format.....	34
4.	Future Experiments.....	36
III.	BASIC FEL THEORY.....	39
A.	RESONANCE.....	43
B.	ELECTRON MOTION.....	47
C.	OPTICAL WAVE EQUATION.....	54
D.	SHORT PULSES.....	61
E.	GAIN.....	64
F.	TAPERED UNDULATOR.....	78
G.	EFFICIENCY.....	82
IV.	TJNAF UPGRADE SIMULATIONS.....	89
A.	20 kW SIMULATIONS.....	91
1.	Gain.....	93
2.	Power.....	96
3.	Energy Spread.....	98
4.	Conclusions of 20kW Simulations.....	100
B.	10 kW SIMULATIONS.....	101
1.	Power.....	102
2.	10 kW Simulation Conclusions.....	106
V.	TAPERING.....	107
A.	EFFICIENCY AND ENERGY SPREAD.....	109
B.	NO TAPER.....	110
C.	POSITIVE TAPERING.....	113
D.	NEGATIVE TAPER.....	120
E.	CONCLUSIONS OF THE CONVENTIONAL AND TAPERED UNDULATORS.....	125
	LIST OF SYMBOLS.....	127
	LIST OF REFERENCES.....	131
	INITIAL DISTRIBUTION LIST.....	135

THIS PAGE INTENTIONALLY LEFT BLANK

LIST OF FIGURES

Figure 1.	Slip-Cast Fused Silica	20
Figure 2.	Damage to Slip-Cast Fused Silica Run 4.....	22
Figure 3.	Polyimide Fiberglass (Front View).....	30
Figure 4.	Polyimide Fiberglass (Back View).....	30
Figure 5.	FEL Undulator in a Resonator Cavity.....	39
Figure 6.	Simulation of Short Pulse Evolution in the FEL.....	62
Figure 7.	Simulation of Phase Space Plot of 20 Electrons.....	72
Figure 8.	Weak Field Gain Spectrum.....	76
Figure 9.	Phase Space Evolution for 20 Electrons.....	77
Figure 10.	TJNAF FEL.....	90
Figure 11.	Simulation Results Showing Gain.....	94
Figure 12.	Steady State Gains.....	96
Figure 13.	Simulation Results for Conventional Undulator.....	97
Figure 14.	Final Power vs. Desynchronism.....	98
Figure 15.	Energy Spread vs. Desynchronism.....	99
Figure 16.	Power Simulation for Klystron Undulator.....	103
Figure 17.	Final Power, Conventional Undulator.....	104
Figure 18.	Final Power, Weak Klystron Undulator.....	105
Figure 19.	Weak Field Gain Spectrum.....	111
Figure 20.	Gain vs. v_0 in Increasing Optical Field a_0	111
Figure 21.	Phase Space for Conventional Undulator.....	112
Figure 22.	Gain vs. v_0 in Increasing Optical Field a_0	114
Figure 23.	Phase Space Showing $\delta > a_0$	116
Figure 24.	Phase Space Showing $a_0 > \delta$	117
Figure 25.	Phase Space Showing $a_0 \gg \delta$	118
Figure 26.	Separatrix for Positive Tapered Undulator... ..	119
Figure 27.	Phase Space for Positive Tapered Undulator.. ..	120
Figure 28.	Gain vs. v_0 in Increasing Optical Field a_0	122
Figure 29.	Phase Space for an Inverse Tapered Undulator.....	123
Figure 30.	Phase Space for a Negative Tapered Undulator.....	125

THIS PAGE INTENTIONALLY LEFT BLANK

LIST OF TABLES

Table 1.	Absorption Percentage vs. Temp for Metals. (After Ref. 11)	8
Table 2.	Irradiation Results of Slip-Cast Fused Silica..	20
Table 3.	Polyimide Fiberglass Irradiation Results.....	31
Table 4.	20 kW FEL Parameters.....	92
Table 5.	10 kW FEL Parameters.....	101
Table 6.	Dimensionless Variables vs. K.....	102

THIS PAGE INTENTIONALLY LEFT BLANK

ACKNOWLEDGEMENTS

I would like to thank several individuals for the assistance they provided to me in my pursuit of a Ph.D.

First I would like to thank Professor Bill Colson. Completion of the numerous classes, exams, boards, conferences, and this dissertation in the time I was allotted would not have been possible without his guidance and assistance. I also enjoyed the benefits that come from working with an advisor who is internationally known and respected for the work he has done in his area of expertise.

I also want to thank Professor Bob Armstead. It was actually his teaching style and humor that gave me the desire and courage to pursue a Ph.D. in physics instead of continuing my studies of engineering.

I want to thank a fellow Ph.D. student, CDR Ed Tucholski. Though busy with his own studies and research, he never turned away a request for assistance from another student, including myself. His ability to teach physics is probably surpassed only by his desire to do so.

Finally I want to thank my wife Pamela. While I put in full days and most weekends, she maintained a full schedule which included doing most of the parenting of our two children, RJ and Nicole. She also did all of the planning and preparation for our move to Washington, DC, so I could finish this dissertation. I could not have done any of this without her.

THIS PAGE INTENTIONALLY LEFT BLANK

I. INTRODUCTION

Since the end of the Cold War the United States Navy has adopted operational strategies that follow the ideas presented in *From the Sea* and *Forward...From the Sea* [Refs. 1 and 2]. The central idea in those documents is the necessity of a new maritime concept, one in which the Navy plays a fundamental role in shore operations being carried out by our armed forces. As a result Navy ships, submarines, and aircraft can be expected to operate in the littoral regions of enemy territories, with the increased potential for encountering hostile forces. Even with the advanced defensive systems on board most of our surface ships, the decreased reaction times available in littoral operations makes them considerably more vulnerable to anti-ship cruise missiles (ASCMs) and attacks by fast attack boats. Additionally, the close proximity of hostile, neutral, and friendly forces makes precision targeting extremely important.

Building on this new maritime concept, the Chief of Naval Operations recently released the Navy Strategic Planning Guidance (April 2000) which prioritizes the capabilities needed to support such a maritime concept. The priority levels range from Priority (I), "Those capabilities that directly support or enhance the enduring core naval competencies without which severe strategic risk would be

incurred", down to Priority (V), "Those capabilities that directly support or enhance... without which minimal strategic risk would be incurred." [Ref. 3, pgs. 40, 61 and 62]

Listed under priority (I) capabilities are:

- The Fleet-wide, point defense capability to achieve high-probability hardkill against sub- and super-sonic cruise missiles.
- The capability to provide area air and missile defense against emerging threats, including advanced cruise missiles.
- The capability to detect, identify, track and destroy high numbers of small craft in the littorals.

According to the Office of Naval Intelligence (ONI), the trends in ASCMs will include:

- Significant increase in missile terminal velocity from predominately sub-sonic speeds today to predominately supersonic by 2010 and hypersonic by 2020.
- Complex terminal maneuvers and seekers to tax point defense systems.

Additionally, ONI concludes that the capabilities most likely to be encountered include massed small boat attack, unalerted single salvo cruise missile attack, short-range ballistic missiles, and terrorist attacks. [Ref. 3, pgs. 8 and 14] Nearly 70 nations have deployed sea and land launched ASCMs, and 20 nations have air launched ASCMs [Ref. 4, pg. 4].

Super-sonic and highly maneuverable missiles are already held by known hostile nations, including the Russian built SSN-22 Sunburn which has a cruise speed/terminal speed of mach 2.5/mach 4.5 [Ref. 5, pg. 121]. Though the terminal speed alone is probably enough to greatly reduce the effectiveness of most self defense systems, this missile also includes a terminal maneuver. This will reduce the effectiveness of self-defense systems such as the Navy's Close in Weapon System (CIWS), which is especially vulnerable to these maneuvers [Ref. 6, pg. 179].

One of the nations that hold this missile is Iran, which has the land launched version [Ref. 5, pg. 325]. If launched in the Straits of Hormuz, which is approximately 40 nautical miles wide, it would take less than 50 seconds to impact a ship transiting approximately 20 nautical miles away through the central section of the straits. Current self-defense systems would have an extremely difficult time engaging such a threat within the 50 second window, especially if it was an unalerted launch. It is threats such as these that make the idea of a Directed Energy Weapon (DEW) stand out as a possible solution.

One such DEW would be a High Energy Laser. In a study carried out by the National Research Council to determine Technology needed for the Navy and Marine Corps for the years 2000 - 2035, a tunable Free Electron Laser (FEL) is specifically called out as the laser of choice for such a weapon due to its ability to be tuned to wavelengths that

offer minimal atmospheric absorption and scattering [Ref. 6, pg. 184]. A secondary advantage of using a FEL is that its gain medium is a vacuum, therefore there is no requirement for the removal of large amounts of waste heat from the lasing medium as with a solid state laser, or the removal of toxic effluents associated with chemical lasers.

Several topics are presented in this dissertation on the use of a FEL as a Directed Energy Weapon. Chapter II discusses the results of material damage experiments conducted at Thomas Jefferson National Accelerator Facility (TJNAF) using a FEL. Some of this work was originally presented by the author at the 21st International FEL Conference in Hamburg, Germany, and is expected to be published in Ref. 7.

Chapter III discusses classical FEL Theory. Starting with the Lorentz force equation and Maxwell's wave equation, the dimensionless FEL pendulum and wave equations are developed [Ref. 29]. The work in this thesis includes modifications of the FEL interactions and gain to include short pulse effects and tapering are also developed, including a modified pendulum equation to include the effects of tapering of the undulator. This work was presented by the author at the 21st International FEL Conference in Hamburg, Germany and was published in Ref. 8. More recent results from simulations conducted by the author were presented at the 22nd International FEL Conference in Raleigh, NC, and will be published in Ref. 7.

Chapter IV includes the results of computer simulations for proposed output power upgrades to the TJNAF FEL. These upgrades are the next step in a proposed upgrade to 1 MW output power. This work was analyzed by the author and was presented at the 20th International FEL Conference in Williamsburg, VA, and 22nd International FEL Conference in Raleigh, NC. Results from 20 kW simulations were published Ref. 9, and results for the 10 kW simulations will be published in Ref. 7.

The last chapter discusses the effect of tapering the undulator, and specifically calls out the differences and advantages of positive vs. negative taper. Simulations conducted by the author resulted in surprising positive results, and were presented by him at the 21st and 22nd International Free Electron Laser Conferences, and published in Refs. 7 and 8.

THIS PAGE INTENTIONALLY LEFT BLANK

II. MATERIAL DAMAGE EXPERIMENTS

A. THEORY

The interaction between lasers and matter is a complicated issue generally described by non-linear and unpredictable effects. The basic kill mechanism for destroying a missile is to cause a catastrophic failure of one of the central components such as the warhead, control and navigation electronics, or the high pressure chamber in the propulsion section, or to create aerodynamic instability beyond the design limits of the missiles flight control surfaces. [Ref. 10]

The laser beam has the unique ability to deliver very high power per unit area. As the optical energy strikes the surface, it is partially absorbed and partially reflected. For metal surfaces and metal alloys, the reflectivity is typically very high (92% or greater) at room temperature. However, for metals interacting with infrared wavelength radiation, there is a decrease in reflectivity with temperature, with an abrupt drop in reflectivity as the material changes from solid to liquid state as shown in Table 1. T_{sl} is the melting temperature of the metal. [Ref. 11.] This loss of reflectivity causes a large increase in the amount of energy absorbed, which results in an even faster increase in temperature. Provided the amount of energy added is greater than the rate of energy diffusion to

surrounding cooler areas, the surface will become hotter and hotter and change from solid to liquid and finally become vaporized.

Table 1. Absorption Percentage vs. Temp for Metals. (After Ref. 11)

Metal	T_m (K)	Absorption at 300 K	Absorption at T_m (Solid)	Absorption at T_m (Liquid)	Absorption at $T_m + 500K$
Ag	1234	0.4%	2.0%	4.3%	5.4%
Al	933	1.1%	4.4%	10.0%	13.0%
Au	1336	0.6%	3.5%	8.3%	10.3%
Cu	1356	0.5%	2.8%	5.8%	7.3%

For typical radome materials there are basically two mechanisms of destruction. The first is penetration by melting and ablating the material. The second is to create fractures by thermally stressing the material. Additionally, if the missile housed an infrared seeker, the radome would naturally be transparent in the infrared. In that case, destruction of the radome would not be necessary. Instead, the infrared laser would penetrate the radome and interact directly with the guidance system and other parts behind the radome. [Ref. 12]

Some of the physical processes that govern the damage caused to the material by the laser include absorption and reflection, density of the material, heat capacity, and thermal conduction. Furthermore, the characteristics of the laser such as irradiation wavelength, power density, peak power, average power, and pulse characteristics play an important role as well.

1. Required Power to Destroy Target

One of the major reasons behind the experiments discussed in this chapter was to determine just how much power from a short-pulse FEL is needed to destroy a missile in the few seconds allowed for an engagement.

One can estimate the required irradiance by assuming that the laser burns through the material by breaking the cohesive bonds of individual atoms allowing the removal of the atoms. In actuality, the matter would most likely disintegrate in "chunks" of atoms. When the laser beam strikes the missile, not all the energy is absorbed, and even some of the absorbed energy makes its way to cooler parts of the material prior to melting. Additionally, some of the power may be wasted by heating some of the atoms beyond the temperature needed to remove them.

One of the materials irradiated during the experiments was aluminum. Metals such as aluminum could be expected to make up the body casing of a cruise missile. The binding

energy of aluminum is approximately 3.4 eV/atom [Ref. 13, pg. 74]. If the casing is assumed to be 3 layers thick, with each layer approximately 1 cm thick, and the laser spot size on the target is 100 cm², the volume of material to be removed is approximately 300 cm³. The atomic spacing for aluminum is approximately 2.5 angstroms [Ref. 13. pg. 98], or 2.5 x 10⁻⁸ cm, which corresponds to the total number of atoms to be removed

$$\frac{300 \text{ cm}^3}{(2.5 \cdot 10^{-8} \text{ cm})^3 / \text{atom}} \approx 2 \cdot 10^{25} \text{ atoms.} \quad (1.)$$

The total energy required is therefore estimated at

$$E = (2 \cdot 10^{25} \text{ atoms})(3.4 \text{ eV} / \text{atom})(1.6 \cdot 10^{-19} \text{ J} / \text{eV}) \quad (2.)$$

$$\approx 10 \text{ MJ}$$

To deliver 10 MJ of energy in 3 to 4 seconds requires approximately 3 MW at the target, assuming all the energy is absorbed. Three MW divided over 100 cm² gives a required irradiance of $\Phi = 30 \text{ kW/cm}^2$. The actual required irradiance level would be determined by the amount of reflected energy.

A second method to estimate the required irradiance is to determine the amount of energy needed to bring the material to its vaporization temperature. If that the energy is delivered at a rate much greater than the heat

loss through diffusion, the required energy can be determined from

$$\Phi_o = \rho z (C[T_m - T_o] + \Delta H_m + C[T_v - T_m] + \Delta H_v) \quad (3.)$$

where Φ_o is the required flux density, ρ = mass density, z = thickness of material to be burned through, C = Specific Heat, T_m = melting temperature, T_o = ambient temperature, T_v = vaporization temperature, ΔH_m = latent heat of melting, and ΔH_v = latent heat of vaporization [REF. 14, pg. 167]. For aluminum the specific values are $\rho = 2700 \text{ kg/m}^3$, $z = 3 \text{ cm}$, $C = 896 \text{ J/kg-K}$, $T_m = 855 \text{ K}$, $T_o = 300 \text{ K}$, $T_v = 2750 \text{ K}$, $\Delta H_m = 4 \times 10^5 \text{ J/kg}$, and $\Delta H_v = 10.8 \times 10^6 \text{ J/kg}$. For this rough estimate the same value for specific heat has been used for both the solid and liquid phases, although in actuality these numbers may be different. Using these values in equation (3.) gives a required flux density of

$$\Phi_o \approx 1 \text{ GJ / m}^2 \quad (4.)$$

or

$$\Phi_o \approx 100 \text{ kJ / cm}^2 \quad (5.)$$

This much energy delivered over a 3 second engagement requires an irradiance of approximately $\Phi_o = 35 \text{ kW/cm}^2$, corresponding to a total beam power of 3.5 MW in a 100 cm^2

spot on the target. This result is consistent with the 3 MW estimate developed with the first approximation method.

A second material irradiated during the experiments was Slip-Cast Fused Silica, a furnace tile material. The specific parameters are $\rho = 2200 \text{ kg/m}^3$, $z = 3 \text{ cm}$, $C = 920 \text{ J/kg-K}$, $T_m = 1980 \text{ K}$, $T_0 = 300 \text{ K}$, $T_v = 2200 \text{ K}$, $\Delta H_m = 1.5 \times 10^6 \text{ J/kg}$, $\Delta H_v = 2.2 \times 10^6 \text{ J/kg}$. Using these numbers in equation (3.) shows that 35 kJ/cm^2 , corresponding to 10 kW/cm^2 over a 3 to 4 second irradiation in order to burn through the material. This is three times smaller than for aluminum because the latent heat of vaporization for aluminum is five times that of the silica, and the vaporization temperature of aluminum is also higher. The thickness of the Slip-Cast Fused Silica used in the experiments was actually only 9 mm, about 1/3 of the thickness of the aluminum used in this example. Calculating the required energy for the 9 mm sample shows that the total energy needed is only 11 kJ/cm^2 , corresponding to a required irradiance of approximately $\Phi_0 = 3 \text{ kW/cm}^2$ for a 3 to 4 second engagement.

These approximations should provide a good estimate of the energy that is actually needed to melt through the missile. As reported later in this chapter, an irradiance level of 10 kW/cm^2 was enough to melt through an aluminum sample that was cut to the correct size in order to control the thermal diffusion. However, when a sample of Slip-Cast Fused Silica was irradiated at the same irradiance level,

burn through was only achieved after an extended time of almost two minutes. A possible explanation for this will be discussed later in this chapter.

Experiments conducted in the 1970's and 1980's in conjunction with the MIRACL program indicate that a power density in the tens of kilowatts is needed to destroy a missile with a dwell time of a few seconds. Experiments conducted by the Air Force during the same time period determined that a flux of 50 kW/cm^2 was needed to damage the missile structure in less than one second [Ref. 15]. Both of these sets of tests seem to validate the order of magnitude approximations made in this section. For this reason most of the experiments discussed later in the report were conducted at an irradiance level of approximately 10 kW/cm^2 .

2. Scaling Laws and Minimal Spot Size

Since there is no MW-class FEL to perform full-scale experiments, scaling is the only way to determine the effectiveness of a FEL weapon. As discussed in the previous section, a power density of approximately $\Phi = 10 \text{ kW/cm}^2$ over a spot size $A \approx 100 \text{ cm}^2$ is required to destroy a missile with a dwell time of a few seconds. Scaling laws would allow predictions of large area damage from small area experiments with the confidence that the two were correlated correctly.

To achieve a power density of $\Phi = 10 \text{ kW/cm}^2$, a 100 W FEL must use a spot size of 1 mm^2 , while a 1 kW laser uses a larger spot size of 10 mm^2 . Scaling of the laser damage will only work if the thermal diffusion is independent of spot size, which is only true for laser spots larger than the characteristic length for thermal diffusion. Schriempf [Ref. 16] calculates the characteristic thermal diffusion length to be

$$D_L = 2\sqrt{\kappa t_e} \quad (6.)$$

where $\kappa = K/\rho C$ is the thermal diffusivity and

$$t_e = \frac{\pi K^2 \Delta T^2}{4\Phi_0^2 K}, \quad (7.)$$

where t_e is the time required to bring the material from ambient temperature to melting temperature, K is the thermal conductivity, ΔT is the temperature change required to reach melting temperature, and Φ_0 is the energy flux being absorbed by the material. The thermal diffusion length D_L represents the distance required for temperature T to drop to $1/e$ times its central value. In the semi-infinite approximation used by Schriempf, radial heat flow is ignored. In order for this to be valid, the spot size must be much larger than D_L , or the target diameter smaller than

D_L , diameter $\leq D_L$. If these conditions are not met, heat will diffuse away from the laser spot, and the area will not be heated effectively.

3. Pulse Train

FELs produce short, powerful pulses with a rapid repetition rate in the MHz range. This can be compared with the typical high peak power short pulse lasers that operate at very low repetition rates of Hz or kHz.

When the laser power is delivered in pulses, the peak power increases and may cause new effects beyond thermal heating. Short pulsed lasers (microseconds and shorter), and ultra-short pulsed lasers (picoseconds and shorter) are capable of producing impulse damage in addition to the thermal damage. The high peak power can cause rapid vaporization at the target surface, and subsequent recoil from the vapor blowoff can form a strong pressure wave. The pressure wave forms a reflected wave at the backside of the material, and the superposition of the two waves can overstress the material and cause catastrophic failing of the material. [Ref. 17]

Another effect occurs where an ultra-short laser pulse delivers energy to a metal at such a fast rate that the metal lattice cannot respond, but the electrons can. The electrons rapidly increase in temperature so that the

difference between electron and lattice temperatures can be as much as a few thousand degrees. [Ref. 18]

Experiments have shown that the damage threshold fluence, E_{th} , of a material gets smaller as the pulse length gets smaller. Experiments show that there may be as much as a factor of 10 advantage when using shorter picosecond pulses over the larger 100 nanosecond pulses. [Ref. 19]

Research has also examined the threshold for ultra-short pulses damaging dielectrics. The same trend as was observed with metals was observed in the dielectrics. For the longer pulses, the damage threshold decreases with decreasing pulse length t_p as $t_p^{1/2}$, down to very short, picosecond pulses. [Refs. 20, 21]

In the experiments conducted at TJNAF, the higher fluence pulses contained 0.12 J/cm^2 of energy, which is slightly higher than the ablation threshold for picosecond pulses on metals [Ref. 22]. Some ablation of the material may have taken place. However, the fluence level was not high enough to create the impulse damage and pressure waves discussed in the paragraphs above.

B. MATERIALS USED IN EXPERIMENTS

In addition to the aluminum samples tested in the experiments, five other materials were also used. The materials chosen were either actual missile nose cone

materials, or materials that were very similar to missile nose cones. The materials are [Refs. 23, 24]:

1. Phenolic Resin:

Radome material from a Standard ARM Missile.

2. Pyroceram:

A furnace coating type material used in SM-1 and SM-2 missile radomes.

3. Slip-Cast Fused Silica:

Commercially available furnace material. Similar to material used as a radome for Patriot missile system.

4. Polyimide Fiberglass:

A high temperature fiberglass used on supersonic missile radomes.

5. F2 Epoxy:

Five plies of fiberglass cloth with an epoxy binder. This type of material is used in the Soviet STYX type missiles.

1. Thermal Diffusion Calculations

The first step in preparing for the experiments was to calculate the thermal diffusion length for each material. The first calculation and test was made for a small piece of aluminum (Al-6061). This material had density $\rho = 2700$ kg/m³, specific heat $C = 896$ J/kg-K, thermal conductivity $K = 180$ W/m-K, thermal diffusivity $\kappa = 7.44 \times 10^{-5}$ m²/s,

melting temperature $T_m = 855\text{K}$, and power density $\Phi_0 = 10^8 \text{ W/m}^2 = 10 \text{ kW/cm}^2$. From equation (6.), the thermal diffusion length is $D = 2 \text{ mm}$, with a time $t = 0.01$ seconds required to begin the melting process. In order to melt through an aluminum sample, the laser spot must have an area greater than $\pi(2 \text{ mm})^2 \approx 10 \text{ mm}^2$. This would make the spot large enough so that the heat arriving at the center of the spot would not be able to diffuse to the cooler regions outside the spot before melting could occur. Alternately, the target itself can be made small with the diameter of the sample diameter $\approx D$ so as to prevent the heat from escaping to cooler regions of material before heating could take place.

These calculations were experimentally verified with samples of Al-6061. A sample with a 1 cm diameter was irradiated with a laser spot size of 1 mm^2 (much smaller than the required 10 mm^2) without melting after several minutes. Other samples with a diameter of 2 mm (very close to the laser spot size itself) were melted in a few seconds.

Another target irradiated was Slip-cast Fused Silica (SiO_2). A calculation of the thermal diffusion length associated with heating the sample to its melting temperature of 1980 K was performed using values $\rho = 2200 \text{ kg/m}^3$, $C = 920 \text{ J/kg-K}$, $K = 1.26 \text{ W/m-K}$, $\kappa = 5 \times 10^{-7} \text{ m}^2/\text{s}$, $T_m = 1980\text{K}$, $\Phi_0 = 10^8 \text{ W/m}^2 = 10 \text{ kW/cm}^2$. Since this material has a

low thermal diffusivity, its thermal diffusion length is also small, $D_L=0.02$ mm. An insulating material such as fused silica, the scaled laser spot can have an area greater than $\pi(0.02 \text{ mm})^2 = 0.001 \text{ mm}^2$, which was easily attained with the 1 mm^2 or larger beams used at TJNAF.

2. Experimental Results

The experiments conducted from March 1999 through March 2000 are reported in great detail by McGinnis, et al. [Ref. 25] Results from two of the materials are reviewed in this section.

a) Slip-Cast Fused Silica

One of the more thorough tests was conducted on Slip-Cast Fused Silica, SiO_2 . The front of the sample after all irradiations is shown in Figure 1, with the numerical results recorded in Table 2.

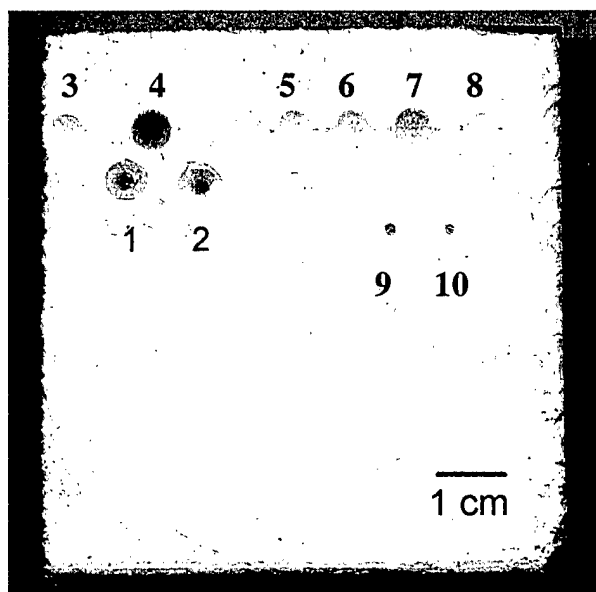


Figure 1. Slip-Cast Fused Silica

Table 2. Irradiation Results of Slip-Cast Fused Silica.

Run Number	Wavelength (μm)	PRF (MHz)	Airflow (mph)	Average Irradiance (kW/cm^2)	Laser Beam Radius (mm)	Penetration Rate (mm/s)
1	3.1	37.4	83-86	10	1.2	1.32
2	3.1	37.4	NO	10	1.2	7.5
3	4.8	37.4	NO	9	0.87	0.2
4	4.8	37.4	NO	9	0.87	0.081
5	4.8	37.4	NO	9	0.87	0.2
6	4.8	37.4	NO	9	0.87	0.125
7	4.8	37.4	NO	9	0.87	0.081
8	4.8	37.4	NO	9	0.87	0.35
9	4.8	37.4	NO	500	0.08	3.0
10	4.8	37.4	NO	500	0.08	3.0

As can be seen in Table 2, there is quite a variation in the penetration rates for the different runs. As the exposure time was increased, more smoke and melted material filled the hole and blocked the path of the laser beam causing the penetration rate to decline over time. Apparently 9 kW/cm^2 is not a high enough irradiance for this material to reach vaporization temperature. The heat was able to diffuse away quickly enough that the material reached a steady state in the liquid form, and would not clear for additional penetration. However, runs 9 and 10 burned through very quickly indicating that 500 kW/cm^2 is more than adequate to bring the material to vaporization temperature.

Since run four was the only run to burn completely through the material at a power density of 9 kW/cm^2 , it is worth a closer look. A digital picture of damage from run four was taken through an optical microscope as shown in Figure 2.

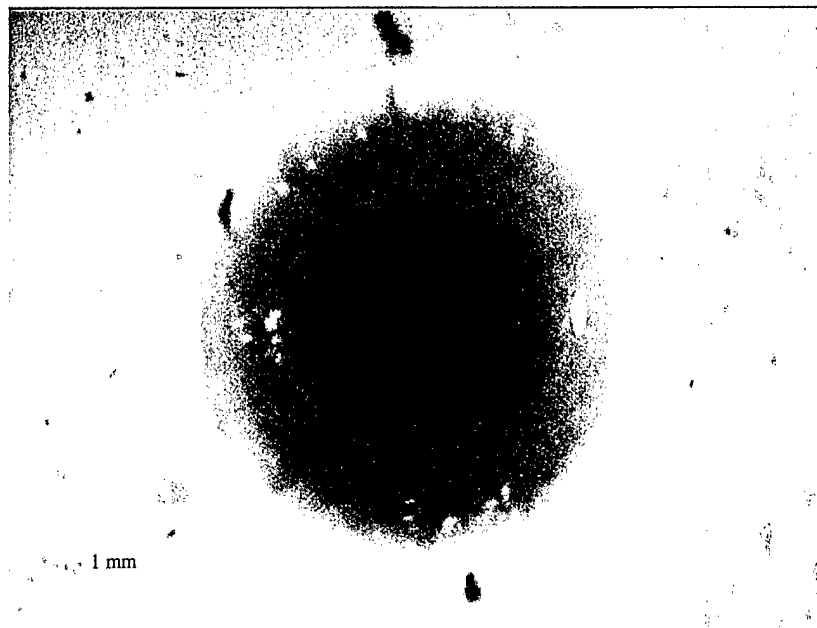


Figure 2. Damage to Slip-Cast Fused Silica Run 4.

The laser beam diameter narrowed from the front surface to the back surface of the hole; its dimensions were 1.1 mm at the front and approximately 0.7 mm at the back. The actual hole (the section of the sample with material had been completely removed during lasing), was very close to those dimensions ranging from 1.06 mm at the front down to 0.7 mm at the back. However, damage to the material was much more wider, with the melted portion at the surface of the sample measuring 5.0 mm in diameter, and the hole at the back edge measuring 2.0 mm in diameter.

Examination of the hole from run four through an optical microscope revealed a 1 mm thick layer of melted and rehardened SiO_2 filling the hole at the back of the sample. It was clear from the video and from the rear power meter

that burn-through occurred in run four, but melted material solidified and resealed the hole at the back of the sample.

The volume of the hole in run four is estimated by,

$$V = \int_0^{9\text{mm}} \pi R^2(z) dz, \quad (8.)$$

where the radius closely matches the laser beam radius and approximately changes linearly as

$$R(z) = 0.53 \text{ mm} - 0.02 z \quad (9.)$$

where z is the distance from the front of the sample. Which gives a volume of $V = 5.6 \text{ mm}^3$ or $5.6 \times 10^{-3} \text{ cm}^3$. By a similar calculation, the volume of the entire damaged region, including the melted and rehardened portion, is estimated to be $V = 92 \text{ mm}^3$. Based on the density of fused silica, $\rho = 2.2 \text{ grams/cm}^3$, the amount of material removed was 0.012 grams, while the amount of material damaged (melted) was 0.20 grams. The heat energy deposited during run four is given by

$$E = Pt = \Phi At, \quad (10.)$$

where $A = \pi(0.53 \text{ mm})^2$, $\Phi = 9 \text{ kW/cm}^2$, and the irradiation time $t = 110 \text{ s}$, so that $E = 9.7 \text{ kJ}$ deposited.

The predictions made in section A.1. of this chapter indicated that this material could be burned through in about 3 seconds at 3 kW/cm^2 , or just over 1 second at the

9 kW/cm² used in these experiments. Using those numbers in equation (10.) gives an estimation of the energy that would need to be deposited to melt through this sample is

$$\begin{aligned} E &= \text{Irradiance} \cdot \text{Beam Area} \cdot \text{time} \\ &= (3 \text{ kW} / \text{cm}^2) \cdot \pi (5.5 \cdot 10^{-2} \text{ cm})^2 \cdot (3 \text{ s}) \\ &= 0.95 \text{ kJ} \end{aligned} \quad (11.)$$

vice the 9.7 kJ that was actually deposited.

The amount of energy needed can also be calculated using the first method in section A.1. That is by calculating the energy needed to break each atomic bond in the volume of the SiO₂ affected. The atomic weight of SiO₂ is 60 amu, or 1×10^{-22} grams. Since the density of SiO₂ is 2.2 grams/cm³, the number of molecules per cubic centimeter is approximately 2×10^{22} . The required energy to break all the bonds assuming approximately 4 eV/bond is estimated as

$$\begin{aligned} E &= (2.2 \cdot 10^{22} \text{ bonds} / \text{cm}^3) (4 \text{ eV} / \text{bond}) (1.6 \cdot 10^{-19} \text{ J} / \text{eV}) \\ &= 12.8 \text{ kJ} / \text{cm}^3. \end{aligned} \quad (12.)$$

From the volume calculated from equation (8.), the total energy required is predicted to be

$$\begin{aligned} E &= (12.8 \text{ kJ} / \text{cm}^3) (5.6 \cdot 10^{-3} \text{ cm}^3) \\ &\approx 0.72 \text{ kJ} \end{aligned} \quad (13.)$$

which is very close to the 0.95 kJ predicted in equation (11.), but far from the 9.7 kJ delivered during the irradiation of run 4.

The difference in the predicted and actual energy requirements may have come about as a result of the change in state of the material. The calculations used in section A.1. of this chapter and in the paragraphs above assume that the thermal diffusion length is small compared to the beam diameter. This assumption is true for Slip-Cast Fused Silica in its normal state, where the thermal diffusion length was calculated in section B.1. to be only 0.02 mm. However, it is possible that once the material melted, the thermal conductivity increased dramatically, increasing the thermal diffusion length substantially. This increase in thermal conductivity would result in a dramatic increase in the rate of heat diffused away from the laser spot, and prevent the material from reaching the vaporization temperature. This increase seems to be what is taking place since even after being irradiated for 110 seconds, the material still contains a large volume of melted and re-solidified material.

This postulate can be checked by calculating the energy deposited during run 9, which was at a much higher irradiance and succeeded in melting through the hole in less than 3 seconds. The amount of energy deposited for this run was

$$\begin{aligned}
 E &= \text{Irradiance} \cdot \text{Beam Area} \cdot \text{time} \\
 &= (500 \text{ kW} / \text{cm}^2) \cdot \pi(8.0 \cdot 10^{-3} \text{ cm})^2 \cdot (3 \text{ s}) \quad (14.) \\
 &= 0.3 \text{ kJ},
 \end{aligned}$$

again showing an amount of energy much smaller than the $\approx 10 \text{ kJ}$ deposited during burn through for run 4. This reinforces the postulate that the energy must arrive at a rate high enough to raise the temperature of the material to vaporization temperature before the molten material can re-solidify. It appears that almost the entire 9.7 kJ of energy delivered during run 4 was wasted because it was delivered too slowly.

In a realistic directed energy application, the irradiance used in run 9 would not be needed. A much larger spot size of 100 cm^2 would not allow for significant thermal diffusion away from the damaged area.

The final experiments were conducted in March 2000. The purpose of the March 2000 experiments was to increase the size of the laser beam spot while maintaining the same irradiance of approximately 10 kW/cm^2 . To do this the average beam power was increased to 500 Watts. Air flow was also added to these experiments to determine if airflow across the material would effect the damage process.

Burn-through of the material occurred for both of the runs conducted to the Slip-Cast Fused Silica during this experiment. The burn-through time for run 1 was 6.8 sec and for run 2 was 1.2 sec. In run 1, the damage diameter on the

front face of the material sample was 4.4 mm, and on the back face was 3.1 mm. In run 2 the damage diameter on the front face was 5.6 mm and on the back face 1.8 mm. The effect of airflow was to reduce the front face damage diameter and to increase the burn-through time.

The volume of the entire damaged region in run 1 is estimated by,

$$V_{1T} = \int_0^{9\text{mm}} \pi \cdot R_{1T}^2(z) \cdot dz, \quad (15.)$$

where z is the depth of the hole. The radius changes approximately linearly as

$$R_{1T}(z) = 2.2\text{mm} - 0.07 \cdot z \quad (16.)$$

The volume of the entire damaged region in run 2 is also estimated by equation (15.), where the radius changes approximately linearly as

$$R_{2T}(z) = 2.8\text{mm} - 0.21 \cdot z \quad (17.)$$

After doing the above calculations, the volume of the entire damage region in run 1 is $V_{1T}=100 \text{ mm}^3$ and in run 2 is $V_{2T}=105 \text{ mm}^3$. The density of the fused silica is $\rho=2.2 \text{ grams/cm}^3$, therefore mass of the entire damaged region in run 1 is $m_{1T}= 0.22 \text{ grams}$ and in run 2 is $m_{2T}=0.23 \text{ grams}$.

The volume of the holes in runs 1 and 2 are estimated using radii

$$R_{1H}(z) = 1.6\text{mm} - 0.17 \cdot z \quad (18.)$$

and

$$R_{2H}(z) = 0.75\text{mm} - 0.04 \cdot z \quad (19.)$$

The calculated volumes of the hole in run 1 is $V_{1H}=35 \text{ mm}^3$ and in run 2 is $V_{2H}=8.9 \text{ mm}^3$. The mass of the material removed creating a hole in run 1 is $m_{1H}=0.08$ grams and in run 2 is $m_{2H}=0.02$ grams.

These calculations show that the addition of air flow had a negligible effect on the overall damaged regions, since both have approximately the same volume. Air flow was substantial in affecting the amount of material removed since the hole volume increased from $V_{2H}=8.9 \text{ mm}^3$ to $V_{1H}=35 \text{ mm}^3$ when the air flow was blowing across the material. However, the air flow also decreased the burn through rate. So, though the hole was bigger, it took longer to create.

Comparing the results of the runs 1 and 2 from the March 2000 experiments with those of runs 3 through 8 in Table 2, it can be seen that shifting the wavelength from $\lambda=4.8 \text{ }\mu\text{m}$ to $\lambda=3.1 \text{ }\mu\text{m}$, and increasing the average power from 100 Watts to 500 Watts had a significant effect on the penetration rates. Those penetration rates increased

dramatically from 0.081 mm/s to 1.32 mm/s with the presence of airflow and to 7.5 mm/s without it.

A possible explanation for the success of the March 2000 runs is the increase in beam radius from 0.087cm to 0.12cm. This increase in beam area could be enough so that even with the larger thermal diffusion length estimated in the preceding paragraphs, the new beam area was large enough to ensure enough heat was retained to reach vaporization.

b) Polyimide Fiberglass

Experiments were also conducted using Polyimide Fiberglass. The front and back of the sample after all experiments were conducted are shown in Figure 3 and Figure 4. Table 3 shows the data for all the experiments conducted on this material over the year long period. Note that runs 10 through 15 were conducted at 500 W/cm², while all the other runs were conducted at 10 kW/cm².

In Figure 4, we see the backside of the sample showing that all of the 10 kW/cm² irradiations completely penetrated the sample. (Note: Hole 3 in Figure 3 has mistakenly been numbered 2 in Figure 4). As can also be seen, none of the 500 W/cm² irradiance runs (irradiations 10 to 15 of Figure 3) penetrated the sample.

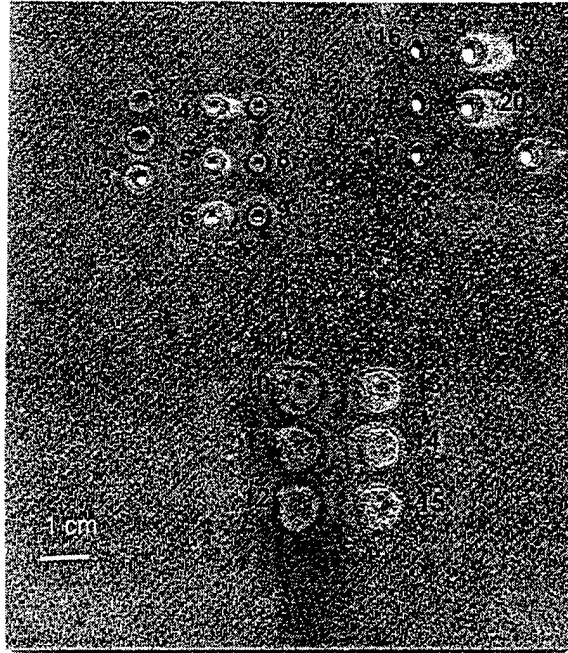


Figure 3. Polyimide Fiberglass (Front View).

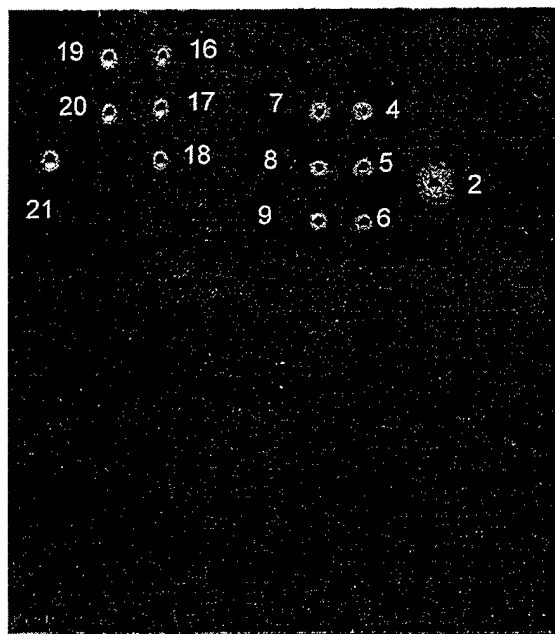


Figure 4. Polyimide Fiberglass (Back View).

Table 3. Polyimide Fiberglass Irradiation Results.

Hole Number	Average Power (W)	Average Irradiance (kW/cm ²)	PRF (MHz)	λ (μm)	Spot radius (mm)	Air flow (mph)	Burn through time (sec)	Penetration Depth Rate (mm/sec)	Front Damage Pattern	Entry Hole Diameter (mm)	Rear Damage Pattern	Exit Hole Diameter (mm)
1*,2*,3	100	10	37.4	4.83	0.55	NO	7	0.28	Circular	3.0	Circular	1.5
4,5,6	100	10	18.7	3.1	0.87	60	1.2	1.6	Circular	1.9	Circular	1.4
7,8,9	100	10	18.7	3.1	0.87	NO	1.4	1.4	Circular	1.7	Circular	1.3
10,11,12	100	0.5	18.7	3.1	2.5	NO	2.5 *	0.3	Circular	4.4	---	---
13,14,15	100	0.5	18.7	3.1	2.5	60	2.5 *	0.3	Circular	6.6	---	---
16,17,18	500	10	37.4	3.1	1.25	NO	0.40	5.0	Elliptical	3.5 x 2.5	Elliptical	2.5 x 1.5
19,20,21	500	10	37.4	3.1	1.25	85	0.35	5.7	Elliptical	3.7 x 2.9	Elliptical	2.6 x 1.7

* There was no burn through. The time indicated is the exposure time.

During runs 1 through 3, only run 3 actually burned through the sample. These three runs have the same irradiation parameters with those of runs 7,8, and 9 of Table 3 except for the PRF and the wavelength. Comparing these runs, it appears that the shorter ($\lambda = 3.1\mu\text{m}$) wavelength combined with the lower PRF is much more effective, resulting in 500% higher penetration depth rate. The lower PRF may be more efficient because it has more energy per pulse for the same pulse length.

For the holes that burned through, the presence of airflow resulted in larger holes and an increased penetration depth rate than those attained without air.

The larger spot size irradiations conducted with 500 W average power (runs 16 to 21), caused 3.5 times higher penetration depth rate than the ones using 100 W (runs 4 to 9), even though both were at the same irradiance level, PRF, and wavelength. This could be because the larger spot allows material to exit the region quicker, or because the larger spot better meets the thermal diffusion requirement. Investigation with a microscope reveals that there is no evidence of melted or rehardened material inside the holes.

C. CONCLUSIONS

This chapter describes some of the first measurements of laser damage on missile materials from a newly developed

TJNAF Free Electron Laser. A much more detailed report of all the experiments conducted over a year long period has also been prepared [Ref. 25].

During the experiments conducted on March 12th and March 23rd, 1999, the only parameter changed was the pulse repetition frequency, which caused the pulses used in the later experiments to have twice the fluence per pulse as the pulses on the 12th. The burn through rate for the experiments of March 23rd was faster, and it is postulated that the increase occurred because the higher fluence pulses, containing 0.12 J/cm² in each pulse, was slightly greater than the ablation threshold for picosecond pulses on metal. It is believed that in the experiments of March 12th, the laser was heating the samples to the melting point, whereas during the experiments of March 23rd, each pulse was ablating a small amount of material immediately. [Ref. 22]

1. Approximation Methods

Two approximation methods were developed to help determine the required energy to be delivered to the target. Both methods assumed that the energy was being delivered at a high enough irradiance to overcome any thermal diffusion. Results from estimates and earlier experiments tend to indicate that an irradiance level of approximately 10 kW/cm² will be required to melt through most missile materials.

2. Scaling

The TJNAF FEL, using several hundred watts of continuous average power was used to simulate the damage from a MW-class weapon by focusing the beam to a smaller spot size to increase irradiance. The goal of these experiments was to begin to develop scaling rules that will reliably predict the damage of a larger laser without having to bare the enormous cost of building the large laser first. The experiments showed that the requirement for the laser spot to be larger than the thermal diffusion length is a valid requirement. The burn through rate increases dramatically as the laser beam radius becomes larger than the thermal diffusion. Some of the experiments indicate that care must be taken when calculating the thermal diffusion length, since this value may change as the material changes states.

3. FEL Pulse Format

The extremely short, sub-picosecond pulse length of the FEL beam is a result of the short electron bunches formed as they are accelerated in RF cavities. The TJNAF FEL has a unique pulse format compared to conventional lasers with a rapid sequence of short, powerful pulses. The peak power in each pulse is about 100 MW lasting for only about one-half

picosecond coming at a rate of 37 MHz. Other studies have shown that such ultra-short pulses may give as much as a factor of ten advantage in the reduced fluence required to produce damage [Ref. 20]. The experiments reported in this chapter began to collect data intended to show whether this advantage exists. The results indicate that for a fixed average power level, a lower pulse repetition frequency with the corresponding higher power per pulse provides a faster burn through rate. This is probably because the lower PRF pulses contained enough fluence per pulse to immediately vaporize the material as well as raising it to melting temperature.

As expected there is a strong relationship between the penetration depth rate and the laser irradiance. When the irradiance changed by a factor of 20 ($500 \text{ W/cm}^2 \rightarrow 10 \text{ kW/cm}^2$) the penetration depth rate changed by almost the same factor.

From earlier studies and the experiments reported in this chapter, it appears that there is a possibility of decreasing the fluence required to cause damage to a material with ultra-short picosecond pulses. This would be a most welcome finding for the high energy laser community since more power means more fuel, more weight, and a higher possibility of thermal blooming of the beam as it propagates through the atmosphere.

4. Future Experiments

The TJNAF FEL is scheduled for an upgrade to 10 kW of power. This increase will allow more flexibility in scaling experiments and further tests of scaling itself. Additional experiments that include weighing of the samples before and after each run, new wavelengths, changing wavelengths during irradiation, new pulse formats, and other sample materials would be beneficial. As experimental procedures are refined and the amount of data increases, a more thorough analysis of the FEL damage results and comparison to other lasers will become possible. Additional experiments can explore just how high the laser irradiance needs to be to bring various missile materials to vaporization temperature.

When higher laser power is available in the future, the same irradiations should be conducted with bigger spot radii in order to compare the results and establish a scaling law. It is suggested that thicker samples should also be tested in order to determine if the penetration rate stays the same after the laser beam has penetrated the material several millimeters. Samples should be machined to be only slightly larger than the laser spot so that thermal diffusion cannot occur. Machining the samples to resemble a small nose cone shape may also be important, because different angles of incidence would be included.

Furthermore, a procedure for making the measurements of burn through times more accurate should be established, as they are very important in determining penetration depth rates.

THIS PAGE INTENTIONALLY LEFT BLANK

III. BASIC FEL THEORY

The free electron laser (FEL) has three primary components: a relativistic electron beam, an undulator, and an optical cavity. The energy from the electron beam is coupled to the electromagnetic field stored in the optical cavity to produce a very high power coherent laser beam. A representation of all three primary components of an FEL is shown in Figure 5.

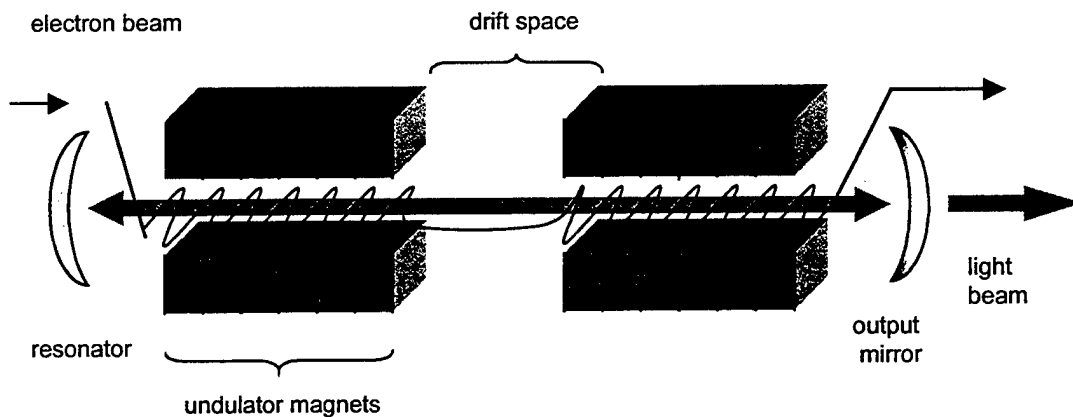


Figure 5. FEL Undulator in a Resonator Cavity

Figure 5 also shows a drift space that is included in some undulator designs. The drift space allows increased gain in the second section of undulator magnets. This design, known as a klystron undulator, will be discussed in chapter IV.

One of the most important qualities of the FEL is the use of a relativistic beam. Since the electrons are moving at speeds close to the speed of light, they experience a Lorentz contracted undulating magnetic field, which results in the emission of electromagnetic pulses at short optical or X-ray wavelengths. [Ref. 26] The emitted wavelength can be calculated by solving for the resonance condition, and is shown later to be approximated by:

$$\lambda \approx \frac{\lambda_0}{2\gamma^2} \quad (20.)$$

where λ = the emitted wavelength, λ_0 = the length of one undulator period, and γ = the Lorentz factor of the relativistic electron beam. A typical FEL will have $\lambda_0 = 5$ cm, and $\gamma = 100$, resulting in an emitted photons with wavelength $\lambda = 2.5 \mu\text{m}$.

At TJNAF, a 350 keV photo-cathode injector generates the electrons. The electrons must be accelerated well above that energy to provide for the short optical pulses desired for a weapon class FEL. The electrons leave the injector and proceed through a RF linear accelerator, where they are accelerated to energy levels of 40+ MeV.

After exiting the accelerators, the electron beam enters the magnetic undulator where it interacts with both the static magnetic field of the undulator, and the dynamic optical field transiting through the undulator at the speed of light. The undulator can be helical or linear, with the helical undulator producing circularly polarized light and the linear undulator producing linear polarized light. The electrons are moving at speeds very close to the speed of light, and are almost in synchronism with the light wave. However, special relativity requires that the finite energy electrons travel slower than the light beam. A condition called resonance is defined as: the electrons are traveling at a speed such that over the distance of one period in the undulator, a light wave of wavelength λ will overtake the electron beam by exactly one wavelength. At resonance, the effects of the moving electrons, the optical wave, and the static magnetic field of the undulator produce a beat wave. This beat wave travels slower than the light wave and is called a ponderomotive wave. At resonance the electrons are actually moving at the same speed as the ponderomotive wave, and the electric field and resulting force the electrons experience is constant and determined by the portion of the ponderomotive wave that they are traveling with. It is this ponderomotive force that causes the electrons to slow down or speed up. [Ref. 27]

The change in speeds of the electrons depending on their phase with respect to the ponderomotive wave causes the electrons to bunch. The bunching is critical if the electrons are to add coherent radiation to the light beam.

The undulator is made from either permanent magnets or electromagnets arranged to create an alternating magnetic field. The polarization can be helical or linear, linear being more common. The purpose of the undulator is to periodically "wiggle" the electrons as they transverse the length of the undulator. This wiggling motion causes the electrons to speed up or slow down (absorb or emit radiation), depending on which part of the ponderomotive wave the electron is in as it is deflected by the undulator.

As with most lasers, the optical cavity stores the light produced by the laser, allowing a fraction to escape on each pass of the light wave. The amount of light that escapes on each pass is usually determined by one of mirrors having a slightly less than perfect reflection coefficient. Allowing too much light to escape results in not enough gain for the laser to operate, while allowing too little light to escape prevents the laser from achieving sufficient output power to destroy a target.

A. RESONANCE

Resonance is described above as the condition where over the length of one period of the undulator, one wavelength of light passes over an electron. Over N such periods of the undulator, the light wave should be a distance of $N\lambda$ ahead of the reference electron. This distance is referred to as the slippage distance, since it represents the distance that an electron has slipped behind the light wave. From this information the wavelength of the light can be calculated. First, the total distance the light wave moves ahead of the electrons is given by:

$$\begin{aligned} N\lambda &= (c - v_z) \Delta t \\ N\lambda &= (c - c\beta_z) \Delta t \\ N\lambda &= c(1 - \beta_z) \Delta t \end{aligned} \tag{21.}$$

where N is the number of undulator periods, λ is the wavelength of the light wave, c = the speed of light, v_z = the speed of the electrons along the line of the undulator, $\beta_z = v_z/c$, and $\Delta t = N\lambda_0/v_z = N\lambda_0/\beta_z c$, the time for the electrons to transverse N undulator periods. Simplifying equation (21.) to solve for the wavelength in terms of velocity in the longitudinal direction:

$$N\lambda = c (1 - \beta_z) \frac{N\lambda_0}{\beta_z c}$$

$$\lambda = \left(\frac{1 - \beta_z}{\beta_z} \right) \lambda_0 \quad (22.)$$

An approximation of the wavelength can be made by using a binomial expansion to determine β_z . The transverse velocity is shown later to be $\beta_1 = \frac{K_u}{\gamma}$, where $K_u = eB\lambda_0/2\pi mc^2$ is the dimensionless undulator parameter. Included in K_u are e , the electron charge magnitude, B , the undulator root-mean-square field strength, λ_0 the undulator wavelength, m the mass of the electron, and c the speed of light. K_u is a dimensionless number that gives a general measure of the magnetic field strength. Continuing with the derivation for optical wavelength with the velocity of the electrons with respect to the velocity of light, β ,

$$\gamma^2 = \frac{1}{1 - \beta^2} = \frac{1}{1 - \beta_1^2 - \beta_z^2} \quad (23.)$$

$$\gamma^{-2} = 1 - \left(\frac{K_u}{\gamma} \right)^2 - \beta_z^2 \quad (24.)$$

$$\gamma^{-2}(1 + K_u^2) = 1 - \beta_z^2 \quad (25.)$$

$$\beta_z^2 = 1 - \frac{(1 + K_u^2)}{\gamma^2} \quad (26.)$$

$$\beta_z = \sqrt{1 - \frac{1 + K_u^2}{\gamma^2}} \approx \left(1 - \frac{1 + K_u^2}{2\gamma^2}\right) \quad (27.)$$

where the last approximation was made by using the binomial expansion since K_u is typically of order unity, and γ^2 of order 10^4 . Inserting this approximation for β_z back into equation (22.), the value for the optical wavelength becomes:

$$\lambda = \left(\frac{1 - \beta_z}{\beta_z}\right) \lambda_o$$

$$\lambda = \frac{\left(1 - 1 + \left[\frac{1 + K_u^2}{2\gamma^2}\right]\right)}{\left(1 - \left[\frac{1 + K_u^2}{2\gamma^2}\right]\right)} \lambda_o \quad (28.)$$

The term in square brackets is very small and can be dropped from the denominator. However, it is the only remaining term in the numerator and must be kept. Therefore, the optical wavelength becomes:

$$\lambda = \left[\frac{1 + K_u^2}{2\gamma^2} \right] \lambda_0 \quad (29.)$$

and since K is usually ≤ 1 ,

$$\lambda \approx \frac{\lambda_0}{2\gamma^2}. \quad (30.)$$

Equation (29.) shows how the optical wavelength can be controlled by three parameters, the undulator wavelength, the undulator parameter, which is primarily controlled by the strength of the magnetic field, and the energy of the electron beam.

The resonance condition used to calculate the approximate wavelength of the light beam is actually not the desired state for the electron beam. At resonance just as many electrons would be absorbing energy from the optical beam and giving energy back to the optical beam. At low gain, the optimum gain condition is for the average electron phase velocity, v_0 , with respect to the ponderomotive wave to be at $v_0 = 2.6$, which means the electrons are initially traveling slightly faster than the ponderomotive wave. This condition will cause the electrons to bunch on the positive slope of the ponderomotive potential, which will cause them

all to slow down (give up energy) together resulting in coherent photon emission.

B. ELECTRON MOTION

Three fields combine to form the ponderomotive wave, producing three forces on the electrons as they move through the undulator. Two of the forces are magnetic. They are caused by the alternating static magnetic field of the undulator, and the moving magnetic field of the optical wave. The third force is from the moving electric field of the optical wave. For a helical undulator the three fields written in CGS units are:

$$\vec{B}_u = B_u (\cos(k_0 z), \sin(k_0 z), 0) \quad (31.)$$

$$\vec{E}_s = E_s (\cos(\psi), -\sin(\psi), 0) \quad (32.)$$

and

$$\vec{B}_s = E_s (\sin(\psi), \cos(\psi), 0) \quad (33.)$$

where B_u is the magnetic field of the undulator, E_s and B_s are the electric and magnetic portions of the optical field, k_0 is the wave number of the undulator, and $\psi = (kz - \omega t + \phi)$ is the phase of the optical wave, where ϕ is the initial phase at $t = 0$ and $z = 0$.

The total force acting on the electron is given by the Lorentz force equations [Ref. 28, pg. 579]. The equations are:

$$\frac{d(\gamma \vec{\beta})}{dt} = -\frac{e}{mc} (\vec{E}_s + \vec{\beta} \times \vec{B}) \quad (34.)$$

and

$$\frac{d\gamma}{dt} = -\frac{e}{mc} \vec{\beta} \cdot \vec{E}_s \quad (35.)$$

Equations (34.) and (35.) are actually four equations. Using these four equations plus equation (23.)

$$\gamma^2 = \frac{1}{1 - \beta^2} = \frac{1}{1 - \beta_1^2 - \beta_z^2} \quad (23.)$$

gives a total of five equations and four unknowns. As is commonly done, since the motion of interest is in the transverse direction, the $\frac{d(\gamma \beta_z)}{dt}$ equation will be ignored.

The transverse components can be written separately as components in x and y as:

$$\begin{aligned}
\frac{d(\gamma\beta_x)}{dt} &= \frac{-e}{mc} (E_{sx} + \beta_z \times B_{uy} + \beta_z \times B_{sy}) \\
\frac{d(\gamma\beta_x)}{dt} &= \frac{-e}{mc} (E_s \cos(\psi) - B_u \beta_z \sin(k_o z) - E_s \beta_z \cos(\psi)) \quad (36.) \\
\frac{d(\gamma\beta_x)}{dt} &= \frac{-e}{mc} (E_s(1 - \beta_z) \cos(\psi) - B_u \beta_z \sin(k_o z))
\end{aligned}$$

and

$$\begin{aligned}
\frac{d(\gamma\beta_y)}{dt} &= \frac{-e}{mc} (E_{sy} + \beta_z \times B_{ux} + \beta_z \times B_{sx}) \\
\frac{d(\gamma\beta_y)}{dt} &= \frac{-e}{mc} (-E_s \sin(\psi) + B_u \beta_z \cos(k_o z) + E_s \beta_z \sin(\psi)) \quad (37.) \\
\frac{d(\gamma\beta_y)}{dt} &= \frac{-e}{mc} (-E_s(1 - \beta_z) \sin(\psi) + B_u \beta_z \cos(k_o z))
\end{aligned}$$

Since $1 - \beta_z \ll 1$, equations (36.) and (37.) can be simplified to:

$$\frac{d(\gamma\beta_x)}{dt} = \frac{-e}{mc} (-B_u \beta_z \sin(k_o z)) \quad (38.)$$

and

$$\frac{d(\gamma\beta_y)}{dt} = \frac{-e}{mc} (B_u \beta_z \cos(k_o z)) \quad (39.)$$

which can be written together as

$$\frac{d(\gamma \vec{\beta}_{\perp})}{dt} = \frac{-eB_u \beta_z}{mc} (-\sin(k_o z), \cos(k_o z), 0) \quad (40.)$$

where the zero has been added to maintain the longitudinal dimension coordinate. By inspection equation (40.) can be integrated to show that:

$$\vec{\beta}_{\perp} = \frac{-K_u}{\gamma} (\cos(k_o z), \sin(k_o z), 0) \quad (41.)$$

The second Lorentz equation is:

$$\frac{d\gamma}{dt} = \frac{-e}{mc} \vec{\beta} \cdot \vec{E}_s \quad (42.)$$

and using equation (32.), this can be written as

$$\begin{aligned} \frac{d\gamma}{dt} &= \frac{-e}{mc} (\beta_x, \beta_y, \beta_z) \cdot (E_s \cos \psi, -E_s \sin \psi, 0) \\ \frac{d\gamma}{dt} &= \frac{-e}{mc} \left(\frac{-K_u}{\gamma} \right) E_s (\cos(k_o z) \cos \psi - \sin(k_o z) \sin \psi) \end{aligned} \quad (43.)$$

Now using the trigonometric identity $\cos(a+b) = \cos(a)\cos(b) - \sin(a)\sin(b)$, this equation simplifies to

$$\begin{aligned}\frac{d\gamma}{dt} &= \frac{eK_u E_s}{mc\gamma} \cos(k_o z + \psi) \\ \frac{d\gamma}{dt} &= \frac{eK_u E_s}{mc\gamma} \cos(\zeta + \phi)\end{aligned}\tag{44.}$$

where $\zeta = (k + k_o)z - \omega t$, the electron phase in the ponderomotive wave.

Next, the time derivative of equation (23.) can be used to get a relation between the time derivative of electron energy, $\dot{\gamma}$, and the time derivative of the fractional velocity, $\dot{\beta}$,

$$\begin{aligned}\gamma^{-2}(1 + K_u^2) &= 1 - \beta_z^2 \\ -2\gamma^{-3}\dot{\gamma}(1 + K_u^2) &= -2\beta_z\dot{\beta}_z \\ \frac{\dot{\gamma}}{\gamma} &= \frac{\gamma^2\beta_z\dot{\beta}_z}{(1 + K_u^2)}\end{aligned}\tag{45.}$$

With $\omega = kc$, the electron phase in the ponderomotive field and its derivatives are:

$$\begin{aligned}\zeta &= (k + k_o)z(t) - \omega t \\ \dot{\zeta} &= (k + k_o)\dot{z} - \omega \\ \dot{\zeta} &= (k + k_o)\beta_z c - \omega \\ \ddot{\zeta} &= (k + k_o)\dot{\beta}_z c\end{aligned}\tag{46.}$$

Therefore,

$$\dot{\beta}_z = \frac{\dot{\zeta}}{(k + k_o)c} \quad (47.)$$

Now, inserting equation (47.) into equation (45.),

$$\begin{aligned} \frac{\dot{\gamma}}{\gamma} &= \frac{\gamma^2 \beta_z \dot{\beta}_z}{(1 + K_u^2)} \\ \frac{\dot{\gamma}}{\gamma} &= \frac{\gamma^2 \beta_z \dot{\zeta}}{(1 + K_u^2)(k + k_o)c} \end{aligned} \quad (48.)$$

and since $\beta_z \approx 1$, $k \gg k_o$, and $kc = \omega$, this becomes

$$\frac{\dot{\gamma}}{\gamma} = \frac{\gamma^2 \dot{\zeta}}{(1 + K_u^2)\omega} \quad (49.)$$

Now using equation (29.) and replacing λ with $\frac{2\pi c}{\omega}$ and λ_o

with $\frac{2\pi c}{\omega_o}$,

$$\omega = \frac{2\gamma^2 \omega_o}{1 + K_u^2} \quad (50.)$$

so that equation (49.) becomes:

$$\frac{\dot{\gamma}}{\gamma} \approx \frac{\ddot{\zeta}}{2\omega_o} \quad (51.)$$

Finally, using equation (44.) for $\dot{\gamma}$:

$$\begin{aligned} \dot{\gamma} &= \frac{\dot{\zeta}}{2\omega_o} \gamma = \frac{eK_u E_s}{mc\gamma} \cos(\zeta + \phi) \\ \ddot{\zeta} &= 2\omega_o \frac{eK_u E_s}{mc\gamma^2} \cos(\zeta + \phi) \end{aligned} \quad (52.)$$

Equation (52.) gives the electron's phase dynamics in the form of a pendulum equation. It governs the electron's phase space motion resulting from the ponderomotive wave. Whenever the total phase $(\zeta + \phi)$ of an electron falls between $\pm \pi/2$, the cosine term will be positive, resulting in an acceleration of that electron. When the phase is between $\pi/2$ and $3\pi/2$, the acceleration is negative. This positive and negative acceleration results in the bunching of the electrons on a scale size of the optical wavelength. The electrons longitudinal motion is approximately limited to $\pm \lambda$. Introducing a the dimensionless variable

$$\tau \approx \frac{ct}{L}$$

where c is the speed of light, t = time, and L is the length of the undulator. The pendulum equation can be rewritten as a second order derivative with respect to τ as

$$\zeta'' = |a| \cos(\zeta + \phi) \quad (53.)$$

where $d\tau = \frac{L}{c} dt$ and $|a| = \frac{4\pi N e K_u L E_s}{\gamma_o^2 m c^2}$. $a = |a|e^{i\phi}$ is called the dimensionless optical field. From equation (53.) it can be seen that the electron motion is a function of the optical field.

C. OPTICAL WAVE EQUATION

In the absence of the optical field, the electrons experience the forces from the undulator field alone. This field causes the electrons to undergo small transverse accelerations, resulting in spontaneous transmissions of photons in the forward direction. The number of electrons in a single pulse is on the order of 10^9 , and the number of photons emitted during the first pass through the undulator is enough that a classical field is formed and then amplified through stimulated emission. [REF. 29, p. 129]

The optical wave equation written in terms of the vector potential is: [Ref. 28, pg. 240]

$$\left[\nabla^2 - \frac{1}{c^2} \frac{\partial^2}{\partial t^2} \right] \vec{A}(\vec{x}, t) \approx - \frac{4\pi}{c} \vec{J}_\perp(\vec{x}, t) \quad (54.)$$

where \vec{J}_\perp is the transverse current density.

The vector potential for a circularly polarized plane wave can be written as a function of z and t only:

$$\vec{A}(z, t) = \frac{E_s(z, t)}{k} [\cos(\psi), -\sin(\psi), 0] \quad (55.)$$

Carrying out the spatial and time derivatives of equation (55.), one obtains

$$\begin{aligned} \frac{\partial^2 \vec{A}}{\partial z^2} &= \frac{1}{k} \frac{\partial E_s}{\partial z} \left(k + \frac{\partial \phi}{\partial z} \right) [\cos(\psi), -\sin(\psi), 0] + \frac{1}{k} \frac{\partial^2 E_s}{\partial z^2} [\sin(\psi), \cos(\psi), 0] \\ &+ \frac{1}{k} \frac{\partial E_s}{\partial z} \left(k + \frac{\partial \phi}{\partial z} \right) [\cos(\psi), -\sin(\psi), 0] + \frac{E_s}{k} \frac{\partial^2 \phi}{\partial z^2} [\cos(\psi), -\sin(\psi), 0] \\ &+ \frac{E_s}{k} \left(k + \frac{\partial \phi}{\partial z} \right)^2 [-\sin(\psi), -\cos(\psi), 0] \end{aligned} \quad (56.)$$

and

$$\begin{aligned}
\frac{\omega}{c} \frac{\partial^2 \vec{A}}{\partial t^2} &= \frac{\partial E_s}{\partial t} \left(\frac{\partial \phi}{\partial t} - \omega \right) [\cos(\psi), -\sin(\psi), 0] + \frac{\partial^2 E_s}{\partial t^2} [\sin(\psi), \cos(\psi), 0] \\
&+ \frac{\partial E_s}{\partial t} \left(\frac{\partial \phi}{\partial t} - \omega \right) [\cos(\psi), -\sin(\psi), 0] + E_s \frac{\partial^2 \phi}{\partial t^2} [\cos(\psi), -\sin(\psi), 0] \\
&+ E_s \left(\frac{\partial \phi}{\partial t} - \omega \right)^2 [-\sin(\psi), -\cos(\psi), 0]
\end{aligned}
\tag{57.}$$

Assuming that the optical phases and amplitudes vary slowly in time and space

$$\frac{\partial E_s}{\partial z} \ll k E_s, \quad \frac{\partial \phi}{\partial z} \ll k \phi, \quad \frac{\partial E_s}{\partial t} \ll \omega E_s, \quad \text{and} \quad \frac{\partial \phi}{\partial t} \ll \omega \phi$$

the second order derivatives are very small and can be eliminated. This allows equation (54.) to be written as:

$$\begin{aligned}
\left[\vec{\nabla}^2 - \frac{1}{c^2} \frac{\partial^2}{\partial t^2} \right] \vec{A}(\vec{x}, t) &= 2 \left(\frac{\partial E_s}{\partial z} + \frac{1}{c} \frac{\partial E_s}{\partial t} \right) [\cos(\psi), \sin(\psi), 0] \\
&+ 2 E_s \left(\frac{\partial \phi}{\partial z} + \frac{1}{c} \frac{\partial \phi}{\partial t} \right) [-\sin(\psi), \cos(\psi), 0] \approx -\frac{4\pi}{c} \vec{J}_\perp(\vec{x}, t)
\end{aligned}
\tag{58.}$$

At this point it is convenient to use the vectors of equation (58.) to define two unit vectors:

$$\hat{\epsilon}_1 = [\cos(\psi), \sin(\psi), 0] \quad \text{and} \quad \hat{\epsilon}_2 = [-\sin(\psi), \cos(\psi), 0]$$

The wave equation (58.) can now be separated into two orthogonal wave equations:

$$\left(\frac{\partial E_s}{\partial z} + \frac{1}{c} \frac{\partial E_s}{\partial t} \right) = - \frac{2\pi}{c} \left(\vec{J}_\perp \cdot \hat{\epsilon}_1 \right) \quad (59.)$$

and

$$E_s \left(\frac{\partial \phi}{\partial z} + \frac{1}{c} \frac{\partial \phi}{\partial t} \right) = - \frac{2\pi}{c} \left(\vec{J}_\perp \cdot \hat{\epsilon}_2 \right) \quad (60.)$$

Still left to be determined is the transverse current. It can be written as the sum of individual electron currents:

$$\vec{J}_\perp(\vec{x}) = -|e|c \sum_i \vec{\beta}_\perp \delta^3(\vec{x} - \vec{r}_i) \quad (61.)$$

where \vec{r}_i is the position of the i^{th} electron with charge e and transverse velocity $\vec{\beta}_\perp c$, and δ^3 is the three dimensional Dirac delta function. Substituting equation (41.) into equation (61.) gives:

$$\vec{J}_\perp(\vec{x}) = -|e|c \sum_i \frac{-K_u}{\gamma} (\cos(k_o z), \sin(k_o z), 0) \delta^3(\vec{x} - \vec{r}_i) \quad (62.)$$

which can be projected onto the two unit vectors defined above to obtain:

$$\vec{J}_\perp(\vec{x}) \cdot \hat{\epsilon}_1 = |e|cK_u \sum_i \frac{\cos(\psi + k_o z)}{\gamma} \delta^3(\vec{x} - \vec{r}_i) \quad (63.)$$

$$\vec{J}_\perp(\vec{x}) \cdot \hat{\epsilon}_2 = |e|cK_u \sum_i \frac{\sin(\psi + k_o z)}{\gamma} \delta^3(\vec{x} - \vec{r}_i) \quad (64.)$$

When the number of undulator periods is very large, $N \gg 1$, then the gain bandwidth curve is very narrow. The change in energy of the electrons per pass through the undulator is very small and therefore the Lorentz factor can be pulled out of the integral.

$$\vec{J}_\perp(\vec{x}) \cdot \hat{\epsilon}_1 = \frac{|e|cK_u}{\gamma} \sum_i \cos(\psi + k_o z) \delta^3(\vec{x} - \vec{r}_i) \quad (65.)$$

$$\vec{J}_\perp(\vec{x}) \cdot \hat{\epsilon}_2 = \frac{|e|cK_u}{\gamma} \sum_i \sin(\psi + k_o z) \delta^3(\vec{x} - \vec{r}_i) \quad (66.)$$

The sum of the product of the individual electrons times the phase of that electron in the ponderomotive potential can be replaced by considering a volume element of

electrons of density ρ_e times the average phase of the potential in that volume element.

$$\vec{J}_\perp(\vec{x}) \cdot \hat{\epsilon}_1 = \frac{|e|cK_u\rho_e}{\gamma} \langle \cos(\psi + k_0 z) \rangle \quad (67.)$$

and

$$\vec{J}_\perp(\vec{x}) \cdot \hat{\epsilon}_2 = \frac{|e|cK_u\rho_e}{\gamma} \langle \sin(\psi + k_0 z) \rangle \quad (68.)$$

Now, rewriting $\psi + k_0 z$ as $\zeta + \phi$, the two orthogonal wave equations (59.) and (60.) become:

$$\left(\frac{\partial E_s}{\partial z} + \frac{1}{c} \frac{\partial_s E}{\partial t} \right) = - \frac{2\pi|e|K_u\rho_e}{\gamma} \langle \cos(\zeta + \phi) \rangle \quad (69.)$$

and

$$E_s \left(\frac{\partial \phi}{\partial z} + \frac{1}{c} \frac{\partial \phi}{\partial t} \right) = \frac{2\pi|e|K_u\rho_e}{\gamma} \langle \sin(\zeta + \phi) \rangle \quad (70.)$$

Equations (69.) and (70.) can be formed from the real and imaginary parts of the following equation:

$$\left(\frac{\partial}{\partial z} + \frac{1}{c} \frac{\partial}{\partial t} \right) E_s e^{i\phi} = - \frac{2\pi|e|K_u\rho_e}{\gamma} \langle e^{-i\zeta} \rangle \quad (71.)$$

Assuming a long electron pulse, there will be no spatial dependence in the z direction, and no longitudinal optical modes are followed. Therefore the $\frac{\partial}{\partial z}$ term can be dropped. [Ref. 29, p 132]

$$\frac{1}{c} \frac{\partial}{\partial t} (E_s e^{i\phi}) = - \frac{2\pi |e| K_u \rho_e}{\gamma} \langle e^{-i\zeta} \rangle \quad (72.)$$

Finally, using the dimensionless variables

$$\tau = \frac{ct}{L}, \quad a = \frac{4\pi |e| K_u L E_s e^{i\phi}}{\gamma^2 mc^2}, \quad \text{and} \quad j = \frac{8N(e\pi K_u L)^2 \rho_e}{\gamma^3 mc^2}$$

the optical wave equation can be written as

$$\dot{a} = -j \langle e^{-i\zeta} \rangle \quad (73.)$$

where \dot{a} is the derivative of the dimensionless optical field, a , with respect to the dimensionless time variable τ . Equation (73.) shows that with no current, or with zero average phase change (no bunching), there is no change in the optical field.

D. SHORT PULSES

Recall that at resonance, the slippage distance was defined as $N\lambda$. Short pulses are defined as pulses whose length is less than or equal to the slippage distance.

In the previous section, the long pulse assumptions were used, basically stating that because the pulse length was larger than the slippage distance, the optical pulse continued to see the same electron density throughout the transition through the undulator over many passes. For short pulses this assumption cannot be made.

Two processes are occurring simultaneously during the passage through the optical cavity. The first process is the electrical pulse slipping backwards with respect to the optical pulse. The second is the bunching that is occurring on the optical wavelength scale. Due to the slippage of the short electron pulses, only the rear section of the optical pulse will remain overlapped with the electron pulse by the time the electrons have achieved bunching. This results in the optical pulse amplification taking place only in the rear of the pulse, while the entire pulse experiences the losses associated with the cavity. The pendulum equation showed that electron motion (phase change) only takes place in the presence of the optical field and is proportional to the magnitude of the optical field.

$$\zeta^{\circ} = |a| \cos(\zeta + \phi) \quad (53.)$$

Since the amplification is only taking place on the rear portion of the optical pulse, the centroid of the pulse grows toward the rear (making the light pulse appear to be moving slower than c) with each pass through the undulator. Eventually, the slower moving optical pulse is entirely off the electron pulse, and no bunching takes place. The optical pulse eventually decays due to the cavity losses. This effect is shown in the left column of Figure 6. The center window of this column shows the optical field, $a(z,n)$, growing strong at $n = 100$, and then decaying again around $n = 350$.

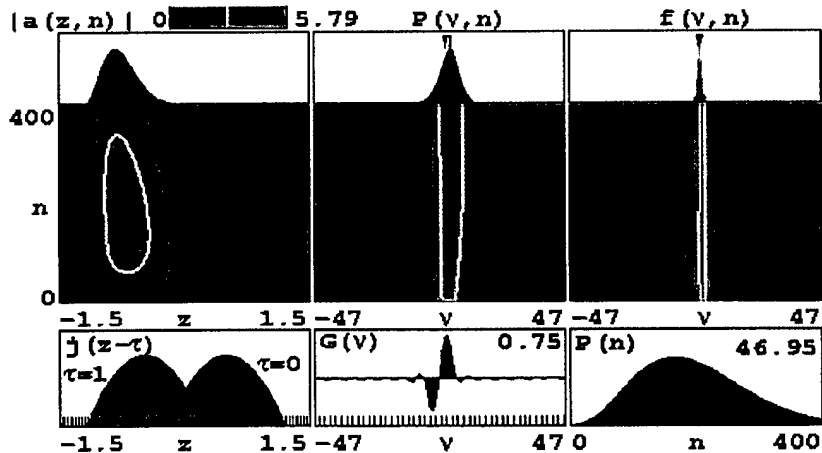


Figure 6. Simulation of Short Pulse Evolution in the FEL.

Figure 6 shows 9 sections arranged in a 3 x 3 grid pattern. The lower left corner indicates the position of the parabolic electron pulse shape. The electron pulse slips back by the slippage distance $N\lambda$ relative to the light pulse as both pulses move through the undulator from $\tau = 0$ to $\tau = 1$. The middle-left plot shows the evolution of the optical field $|a(z,n)|$ as it grows over $n = 400$ passes through the undulator, with the final optical pulse shape shown in the top-left window.

The center graph shows the evolution of the optical power spectrum, $P(v,n)$ over $n = 400$ passes through the undulator, where v is the electron velocity or energy. The top-center plot shows the final optical power spectrum after $n = 400$ passes. The bottom-middle plot is the weak-field gain spectrum, $G(v)$, showing a maximum gain occurring at $v = 2.6$.

The lower-right window shows the Power of the optical pulse $P(n)$. The middle-right plot shows the evolution of the electron spectrum $f(v,n)$ over $n = 400$ passes, while the top-right plot shows the final spectrum after $n = 400$ passes through the undulator.

The electron pulse is timed to enter the cavity in synchronism with the reflected optical pulse, which has a time interval of $2S/c$, where S is the one way distance

between the mirrors of the cavity. However, as the optical pulse starts to move back, the bunching of the electron pulse is delayed more and more, causing the amplification process to take place even further back on the optical pulse. Eventually, the overlap between optical and electron pulses is zero, and the optical pulse decays to zero.

The desynchronism, d , is defined as the displacement between the electron and optical pulses at the entrance to the optical cavity. It is normalized to the slippage distance. $d = 0$ means the pulses are in perfect synchronization. However, since in effect the optical pulse is moving back with each pass, the desynchronism needs to be adjusted so that the "slowed" optical pulse arrives with the electron pulse. This is done by shortening the length of the optical cavity by an amount ΔS , resulting in a desynchronism value of $d = 2\Delta S/N\lambda$.

E. GAIN

FELs are generally operated as either amplifiers or oscillators. Amplifiers are single pass FELs that require high gain to develop high power in one pass through the undulator. Oscillators create their power over many passes and therefore can operate at low gain.

The gain of a FEL is defined as the percentage change in the optical field per pass through the oscillator:

$$G = \frac{a_t^2 - a_o^2}{a_o^2} \quad (74.)$$

where a_t is the optical field strength at the end of the undulator, and a_o is the optical field strength at the beginning of the undulator.

To achieve gain, energy has to be removed from the electron beam and added to the optical beam. Therefore a basic method to analyze the gain in the optical field energy is to determine the change in energy of the electrons, $\frac{\Delta\gamma}{\gamma}$, for each electron, and add these changes together for all the electrons. A negative change in average energy of the electron beam means a positive change in the energy of the optical beam.

The change in energy of a single electron is proportional to its change in phase velocity. The instantaneous phase velocity is given in equation (46.) as:

$$v = \dot{\zeta} = (k + k_o)\beta_z c - \omega \quad (46.)$$

or in units of dimensionless time τ where $\partial t \rightarrow \frac{c}{L} \partial \tau$:

$$\begin{aligned}
\nu &= \dot{\zeta} = \frac{L}{c} [(k + k_o)\beta_z c - \omega] \\
\nu &= \dot{\zeta} = L \left[(k + k_o)\beta_z - \frac{\omega}{c} \right] \\
\nu &= \dot{\zeta} = L[(k + k_o)\beta_z - k]
\end{aligned} \tag{75.}$$

where L = the length of the undulator.

The change in the phase velocity can be written as:

$$\begin{aligned}
\Delta\nu &= \Delta\dot{\zeta} = L(k + k_o)\Delta\beta_z \\
\Delta\nu &= \Delta\dot{\zeta} \approx Lk\Delta\beta_z
\end{aligned} \tag{76.}$$

where the approximation comes from the fact that $k \gg k_o$.

To relate $\Delta\nu$ to $\Delta\gamma$ use the substitutions $L = N\lambda_o$, $k = 2\pi/\lambda$, $k_o = 2\pi/\lambda_o$, and equation (29.)

$$\lambda = \left[\frac{1 + K_u^2}{2\gamma^2} \right] \lambda_o \tag{29.}$$

to obtain:

$$\begin{aligned}
\Delta \nu &= N \lambda_o \left(\frac{2\pi}{\lambda} \right) \Delta \beta_z \\
\Delta \nu &= N 2\pi \left(\frac{\lambda_o}{\lambda} \right) \Delta \beta_z \\
\Delta \nu &= N 2\pi \left(\frac{2\gamma^2}{1 + K_u^2} \right) \Delta \beta_z
\end{aligned} \tag{77.}$$

Now use equation (48.) in difference rather than differential form:

$$\frac{\Delta \gamma}{\gamma} = \frac{\gamma^2 \beta_z \Delta \beta_z}{(1 + K_u^2)} \tag{48.}$$

to substitute $\Delta \beta_z$ into equation (77.)

$$\begin{aligned}
\Delta \nu &= N 2\pi \left(\frac{2\gamma^2}{1 + K^2} \right) \frac{\Delta \gamma}{\gamma^3} \frac{(1 + K_u^2)}{\beta_z} \\
\Delta \nu &= \frac{4\pi N}{\beta_z} \frac{\Delta \gamma}{\gamma} \\
\Delta \nu &\approx 4\pi N \frac{\Delta \gamma}{\gamma}
\end{aligned} \tag{78.}$$

where the last approximation comes from the fact that $\beta_z \approx 1$. The change in energy of the electron is $\Delta \gamma mc^2$ or

$$\Delta E_s = \frac{\Delta v}{4\pi N} \gamma m c^2 \quad (79.)$$

The average energy change, $\bar{\Delta E}_s$, for an electron is:

$$\bar{\Delta E}_s = \Delta \gamma_{\text{Total}} m c^2 = \frac{\langle \Delta v \rangle}{4\pi N} \gamma m c^2 \quad (80.)$$

where $\Delta \gamma_{\text{Total}}$ is the sum total change in energy of the electron beam from all the electrons.

Assuming a monoenergetic beam enters the undulator with phase velocity v_o , this can be rewritten as:

$$\bar{\Delta E}_s = \Delta \gamma_{\text{Total}} m c^2 = \frac{\langle v \rangle - v_o}{4\pi N} \gamma m c^2 \quad (81.)$$

The final term to determine is the average energy term for each electron at the end of the undulator, $\langle v \rangle$. The phase velocity v can be determined by integrating the pendulum equation once

$$v = \int \zeta'' d\tau = \int |a| \cos(\zeta + \phi) d\tau \quad (82.)$$

In weak fields the changes in the optical field, electron phase, and optical phase are small: $\dot{a} \approx 0$ and $\dot{\phi} \approx 0$. In weak fields the pendulum equation can be rewritten by expanding the phase, ζ , in terms of the dimensionless optical field term a

$$\ddot{\zeta} = \frac{\partial^2}{\partial \tau^2} (\zeta^{(0)} + \zeta^{(1)} + \zeta^{(2)} + \dots) = |a| \cos(\zeta^{(0)} + \zeta^{(1)} + \zeta^{(2)} + \dots) \quad (83.)$$

using the zeroth order conditions

$$\begin{aligned} a^{(0)} &= a_0 \\ v^{(0)} &= v_0 + \dots \\ \zeta^{(0)} &= \zeta_0 + v_0 \tau + \dots \end{aligned} \quad (84.)$$

To zeroth order the pendulum equation becomes

$$\ddot{\zeta}^{(0)} = \frac{\partial^2}{\partial \tau^2} (\zeta^{(0)}) = 0 \quad (85.)$$

To first order in 'a' the equations becomes

$$\ddot{\zeta}^{(1)} = \frac{\partial^2}{\partial \tau^2} (\zeta^{(0)} + \zeta^{(1)}) = |a^{(0)}| \cos(\zeta^{(0)}) = a_0 \cos(\zeta_0 + v_0 \tau) \quad (86.)$$

which from equation (85.) is

$$\ddot{\zeta}^{(1)} = \frac{\partial^2}{\partial \tau^2} (\zeta^{(1)}) = a_0 \cos(\zeta_0 + \nu_0 \tau) \quad (87.)$$

Integrating equation (87.) once produces

$$\dot{\zeta}^{(1)} = \nu^{(1)} = \frac{a_0}{\nu_0} [\sin(\zeta_0 + \nu_0 \tau) - \sin(\zeta_0)] \quad (88.)$$

Integrating a second time provides the first order approximation for ζ :

$$\begin{aligned} \zeta^{(1)} &= \frac{a_0}{\nu_0^2} [-\cos(\zeta_0 + \nu_0 \tau) + \cos(\zeta_0)] - \frac{a_0 \tau}{\nu_0} [\sin(\zeta_0)] \\ \zeta^{(1)} &= -\frac{a_0}{\nu_0^2} \{[\cos(\zeta_0 + \nu_0 \tau) - \cos(\zeta_0)] + \nu_0 \tau [\sin(\zeta_0)]\} \end{aligned} \quad (89.)$$

Using these equations the second order approximation of the pendulum equation is:

$$\begin{aligned}
\ddot{\zeta}^{(2)} &= \frac{\partial^2}{\partial \tau^2} (\zeta^{(0)} + \zeta^{(1)} + \zeta^{(2)}) = |a| \cos(\zeta^{(0)} + \zeta^{(1)}) \\
\ddot{\zeta}^{(2)} &= \frac{\partial^2}{\partial \tau^2} \left(\zeta_0 + \nu_0 \tau + -\frac{a_0}{\nu_0^2} \{[\cos(\zeta_0 + \nu_0 \tau) - \cos(\zeta_0)] + \nu_0 t [\sin(\zeta_0)]\} + \zeta^{(2)} \right) \\
&= |a| \cos(\zeta^{(0)} + \zeta^{(1)}) \\
\ddot{\zeta}^{(2)} &= \left(0 + a_0 \cos(\zeta_0 + \nu_0 \tau) + \frac{\partial^2}{\partial \tau^2} (\zeta^{(2)}) \right) = a_0 \cos(\zeta_0 + \nu_0 \tau + \zeta^{(1)})
\end{aligned} \tag{90.}$$

The right side can be expanded by the identity $\cos(a+b) = \cos(a)\cos(b) - \sin(a)\sin(b)$ and by the approximations $\cos(\zeta^{(1)}) \approx 1$ and $\sin(\zeta^{(1)}) \approx \zeta^{(1)}$:

$$\begin{aligned}
a_0 \cos(\zeta_0 + \nu_0 \tau) + \frac{\partial^2}{\partial \tau^2} (\zeta^{(2)}) &= a_0 [\cos(\zeta_0 + \nu_0 \tau) \cos(\zeta^{(1)}) - \sin(\zeta_0 + \nu_0 \tau) \sin(\zeta^{(1)})] \\
a_0 \cos(\zeta_0 + \nu_0 \tau) + \frac{\partial^2}{\partial \tau^2} (\zeta^{(2)}) &= a_0 [\cos(\zeta_0 + \nu_0 \tau) - \sin(\zeta_0 + \nu_0 \tau) (\zeta^{(1)})] \\
\frac{\partial^2}{\partial \tau^2} (\zeta^{(2)}) &= -a_0 \sin(\zeta_0 + \nu_0 \tau) (\zeta^{(1)}) \\
\frac{\partial^2}{\partial \tau^2} (\zeta^{(2)}) &= \frac{a_0^2}{\nu_0^2} \sin(\zeta_0 + \nu_0 \tau) \{ \cos(\zeta_0 + \nu_0 \tau) - \cos(\zeta_0) + \nu_0 t \sin(\zeta_0) \}
\end{aligned} \tag{91.}$$

Integrating equation (91.) once gives:

$$\nu^{(2)} = \frac{a_0^2}{\nu_0^3} \left[-\frac{1}{4} (\cos(2\zeta_0 + 2\nu_0 \tau) - \cos(2\zeta_0)) + \cos(\nu_0 \tau) - \right. \\
\left. 1 - \nu_0 \tau \sin \zeta_0 \cos(\zeta_0 + \nu_0 \tau) \right] \tag{92.}$$

Equations (89.) and (93.) give higher order approximations for the phase and phase velocity of the electrons, which can be represented together in phase space as shown in the large window of Figure 7. This figure shows the phase space position of 20 electrons after transversing the distance of the undulator. About half of the electrons have bunched together at a phase position $\zeta = \pi$.

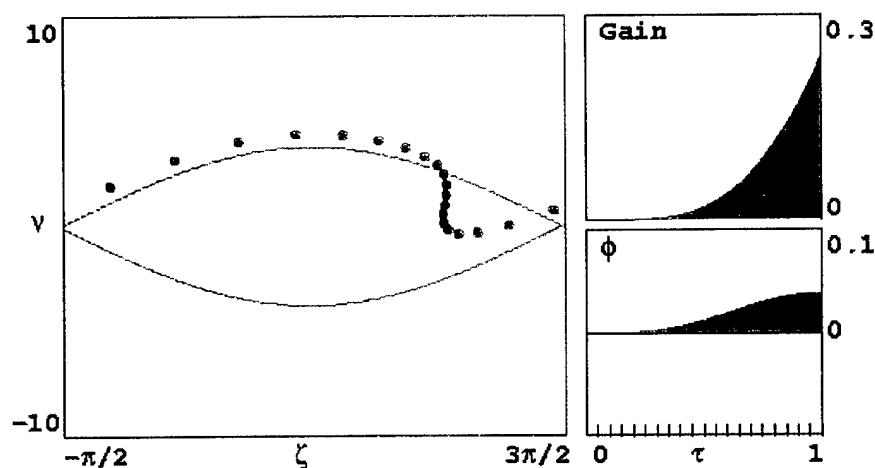


Figure 7. Simulation of Phase Space Plot of 20 Electrons.

In Figure 7 the large window shows the electrons position, ζ , and velocity, v , relative to the ponderomotive wave. This example shows only the final phase space positions of the electrons. The lower right window shows

the evolution in the optical phase, $\phi(\tau)$, and the upper right window shows the gain $G(\tau)$.

Equation (89.) shows that to first order the bunching is proportional to the optical field a_0 , and that some of the electrons move forward while some move backwards, depending upon their initial phase position, ζ_0 and phase velocity, v_0 .

To first order, the final velocity is proportional to a_0 . It is also dependent on initial phase and phase velocity, with some of the electrons gaining energy and some losing energy.

To complete equation (81.), the final unknown $\langle v \rangle$ can be approximated as:

$$\langle v \rangle = \langle v^{(0)} + v^{(1)} + v^{(2)} + \dots \rangle \quad (93.)$$

The electrons enter the undulator with a pulse length that is many optical wavelengths long. The phase space is periodic on the optical wavelength scale, so the average change in energy $\overline{\Delta E_s}$ can be determined over one wavelength:

$$\overline{\Delta E_s} = \sum_i f_i(\zeta_0) = \int_0^{2\pi} f(\zeta_0) \frac{d\zeta_0}{2\pi} \quad (94.)$$

The average for the zeroth order approximation is:

$$\langle \nu^0 \rangle = \nu_0 \quad (95.)$$

indicating no change in average energy of an electron.

To first order the average is:

$$\langle \nu^{(1)} \rangle = \nu_0 + 0 \quad (96.)$$

since the two sine functions in equation (88.) cancel when averaged over all values of ζ_0 .

To second order the average is:

$$\langle \nu^{(2)} \rangle = \nu_0 + 0 + \frac{a_0^2}{\nu_0^3} \left[\cos(\nu_0 \tau) - 1 + \frac{1}{2} \nu_0 \tau \sin(\nu_0 \tau) \right] \quad (97.)$$

which produces a net change in the average energy dependent upon the initial phase velocity of the electron.

Equation (97.) can be placed into equation (81.) to give the average phase velocity change in the electron beam.

The gain in the optical beam was defined as the change in energy of the optical beam divided by the initial energy. It can be determined on the differential volume element dV

level as the change in the energy of the electron beam in that volume, divided by the initial optical beam energy in the same volume. The energy in a volume element containing the optical beam is:

$$\epsilon_{0\text{-beam}} = \frac{2E_s^2}{8\pi} dV \quad (98.)$$

where E is the Electric field of the beam.

The average change in energy per electron is given in equation (97.). The number of electrons in a volume element of light dV is $\rho F dV$, where F is the filling factor, which is the ratio of the electron beam area to the optical beam area. The gain in the optical beam is therefore:

$$G = \left(\frac{d\epsilon_{e\text{-beam}}}{\epsilon_{o\text{-beam}}} \right) = \frac{(\rho F dV) [\gamma mc^2 (\langle \nu \rangle - \nu_0) / 4\pi N]}{2E_s^2 dV / 8\pi} \quad (99.)$$

and using equation (97.) the gain becomes:

$$G = - \frac{4\pi \rho_e F \gamma mc^2}{E_s^2} \frac{a_0^2}{\nu_0^3} \left[\cos(\nu_0 \tau) - 1 + \frac{1}{2} \nu_0 \tau \sin(\nu_0 \tau) \right] \quad (100.)$$

Using the dimensionless variable $j = 8N(e\pi K_u^2 L)^2 \rho_e F / \gamma^3 mc^2$ produces

$$G = \frac{j[2 - 2 \cos(v_0 \tau) - v_0 \tau \sin(v_0 \tau)]}{v_0^3} \quad (101.)$$

Equation (101.) shows that in the weak field low current approximations used here, the gain is primarily a function of initial phase velocity, v_0 . Figure 8 below is a plot of the gain spectrum for a range of phase velocities from - 15 to + 15. Gain G is plotted on the vertical axis, while initial phase velocity v_0 is plotted on the horizontal axis. The computer simulated spectrum shows a peak gain of 27% when the phase velocity equals 2.6. The spectrum is anti-symmetric about $v_0 = 0$, indicating that the maximum loss would occur for a electron beam with a velocity of $v_0 = -2.6$.

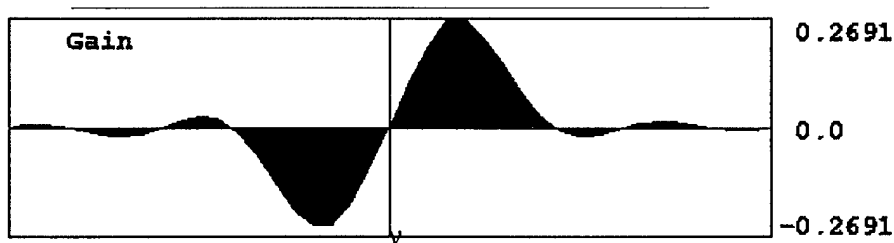


Figure 8. Weak Field Gain Spectrum

A phase space plot showing the evolutions in phase space of 20 electrons with initial phase velocity of $v_0 = 2.6$ is shown in Figure 9. The light colored dots indicate the phase space positions at the beginning of the undulator, and the darker colored dots show the positions at the end. As can be seen in the figure, many of the darker colored dots are bunched in the phase position of approximately $\zeta = \pi$, and are all moving down in phase velocity. This indicates that by the time the electrons reach the end of the undulator, they are bunched together on the optical wavelength scale, and are losing energy to the light beam.

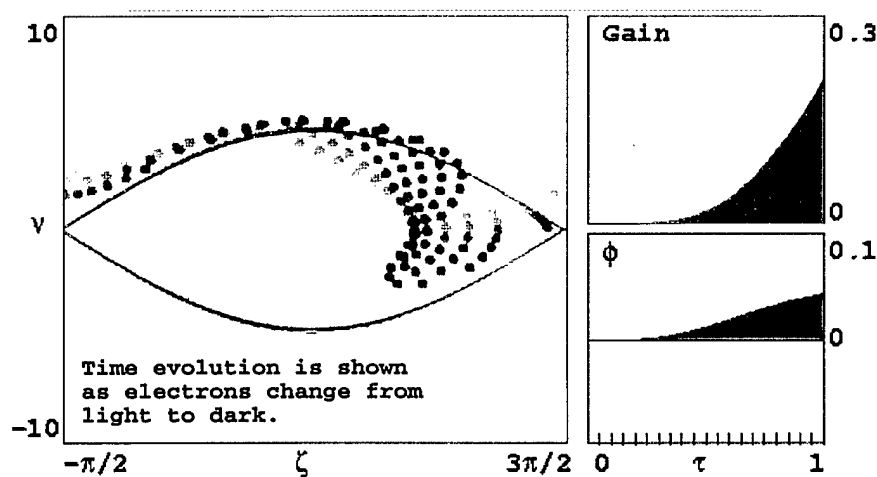


Figure 9. Phase Space Evolution for 20 Electrons.

F. TAPERED UNDULATOR

The resonant condition was defined in equation (29.) as:

$$\lambda = \left[\frac{1 + K_u^2}{2\gamma^2} \right] \lambda_0 \quad (29.)$$

The resonant condition was used to calculate the change in energy expression in equation (78.). However, once the optical beam amplitude becomes large, the change in energy of the electrons is such that they are no longer in resonance with the optical beam and the gain decreases.

One method to maintain resonance and as a result maintain gain is to change one of the parameters in equation (29.), so that the right side of the equation remains constant even with decreasing energy. This can be done by decreasing the undulator wavelength, λ_0 , or by decreasing the magnetic field strength resulting in a decreased value in the undulator parameter K_u . Both methods are referred to as tapering the undulator.

Effectively either one of the changes produces the same effect on the electrons as if the electron had been accelerated back up to the resonance speed by some electrostatic force in the direction of the beam. The acceleration of the electrons is given by the pendulum

equation, and thus the effect of tapering the undulator is included in the modified pendulum equation:

$$\ddot{\zeta} = \delta + |a| \cos(\zeta + \phi) \quad (102.)$$

where δ is the term representing the new 'acceleration' or 'torque' that the tapering of the undulator will cause.

To determine the value of δ that will result from reducing the undulator wavelength λ_0 , start with equation (71.)

$$v = \dot{\zeta} = L[(k + k_0)\beta_z - k] \quad (71.)$$

and calculate the effect that an incremental change in λ_0 will have on the phase velocity v .

$$\begin{aligned} v &= L \left[\left(k + \frac{2\pi}{\lambda_0} \right) \beta_z - k \right] \\ \delta &= \Delta v = L \left[(-1) \frac{2\pi}{\lambda_0^2} \right] \beta_z \Delta \lambda_0 \\ \delta &= \Delta v \approx -2\pi N \frac{\Delta \lambda_0}{\lambda_0} \end{aligned} \quad (103.)$$

where the last line included $L = N\lambda_0$ and $\beta_z \approx 1$. A typical value of the tapering is $\frac{\Delta\lambda_0}{\lambda_0} = -0.2$. If $N = 100$, the value for the acceleration is $\delta = -200\pi(-0.2) = 40\pi$.

The value of δ achieved by a change in the magnetic field strength is determined similarly. Start with equation (45.) to relate the undulator parameter K_u to β_z by using a binomial expansion:

$$\gamma^{-2}(1 + K_u^2) = 1 - \beta_z^2 \quad (45.)$$

$$\beta_z^2 = 1 - \frac{1 + K_u^2}{\gamma^2}$$

$$\beta_z = \sqrt{1 - \left(\frac{1 + K_u^2}{\gamma^2}\right)} \quad (104.)$$

$$\beta_z \approx 1 - \frac{1 + K_u^2}{2\gamma^2}$$

Using this approximation in equation (71.) gives

$$\begin{aligned} \nu &= \dot{\zeta} = L[(k + k_0)\beta_z - k] \\ \nu &= L[k\beta_z - k + k_0\beta_z] \\ \nu &= L[k(\beta_z - 1) + k_0\beta_z] \\ \nu &= L\left[k\left(1 - \frac{1 + K_u^2}{2\gamma^2} - 1\right) + k_0\left(1 - \frac{1 + K_u^2}{2\gamma^2}\right)\right] \\ \nu &= L\left[-k\left(\frac{1 + K_u^2}{2\gamma^2}\right) + k_0\right] \end{aligned} \quad (105.)$$

where the term $\frac{1 + K_u^2}{2\gamma^2} \ll 1$ was dropped from the second parenthesis term, but could not be dropped from the first parenthesis term because it was the only remaining piece. Continuing by making the substitutions $L = N\lambda_0$, $k = \frac{2\pi}{\lambda}$, and using equation (29.) for the value of $\frac{\lambda_0}{\lambda}$ the value for the acceleration term δ is

$$\begin{aligned}
 \delta &= \Delta v = N\lambda_0 \left[-\frac{2\pi}{\lambda} \left(\frac{2K_u}{2\gamma^2} \right) \Delta K_u \right] \\
 \delta &= -4\pi N \frac{\lambda_0}{\lambda} \left(\frac{1}{2\gamma^2} \right) K_u \Delta K_u \\
 \delta &= -4\pi N \left(\frac{2\gamma^2}{1 + K_u^2} \right) \left(\frac{1}{2\gamma^2} \right) K_u^2 \frac{\Delta K_u}{K_u} \\
 \delta &= -4\pi N \left(\frac{K_u^2}{1 + K_u^2} \right) \frac{\Delta K_u}{K_u}.
 \end{aligned}
 \tag{106.}$$

The amount of tapering that can be applied is not unlimited. The general rule is

$$|a| > |\delta| < 4\sqrt{a} > 2\pi$$

The first requirement of $|a| > |\delta|$ ensures that some of the electrons will be trapped in the ponderomotive potential well, known as particle trapping. If a is smaller than δ then the particles will all be accelerated in phase space out and away from the separatrix. The second requirement ensures that the tapering is strong enough to overcome the natural untapered deceleration, and the last requirement ensures that the system is operating in a strong optical field condition where tapering is needed. [Ref. 29, pg. 157]

G. EFFICIENCY

The efficiency η of a Free Electron Laser is defined as the fractional loss in energy of the electron beam during one passage through the undulator.

$$\eta = -\frac{\langle \Delta\gamma \rangle mc^2}{\gamma mc^2} = -\frac{\langle \Delta\gamma \rangle}{\gamma_0} \quad (107.)$$

where $\langle \Delta\gamma \rangle$ is the average energy of an electron at the end of the undulator.

The efficiency of the FEL can be increased by tapering the undulator. Assuming λ, λ_0 , and N are fixed, the effect of tapering $\pm \delta$ can be determined starting with equation (105.)

$$\nu = L \left[k_o - k \left(\frac{1 + K_u^2}{2\gamma^2} \right) \right] \quad (105.)$$

Recalling $L = N\lambda_o$ this can be written in terms of the fixed variables λ, λ_o , and N as

$$\nu = N\lambda_o \left[\frac{2\pi}{\lambda_o} - \frac{2\pi}{\lambda} \left(\frac{1 + K_u^2}{2\gamma^2} \right) \right] \quad (108.)$$

Rearranging terms, the equation can be rewritten as a solution of γ^2

$$\begin{aligned} \nu &= 1 - \frac{\lambda_o(1 + K_u^2)}{2\gamma^2\lambda} \\ \gamma^2 &= \frac{\lambda_o(1 + K_u^2)}{2\lambda \left(1 - \frac{\nu}{2\pi N} \right)} \end{aligned} \quad (109.)$$

For a tapered undulator, $K_u = K_{uo} + \Delta K_u \tau$. Typically, $\Delta K_u \ll K_{uo}$ and $\nu \ll 2\pi N$, so

$$\begin{aligned}
\gamma^2 &= \frac{\lambda_o(1 + K_{uo}^2 + 2K_{uo}\Delta K_u\tau + (\Delta K_u\tau)^2)}{2\lambda\left(1 - \frac{\nu}{2\pi N}\right)} \\
\gamma^2 &\approx \frac{\lambda_o(1 + K_{uo}^2 + 2K_{uo}\Delta K_u\tau)}{2\lambda\left(1 - \frac{\nu}{2\pi N}\right)} \cdot \frac{\left(1 + \frac{\nu}{2\pi N}\right)}{\left(1 + \frac{\nu}{2\pi N}\right)} \quad (110.) \\
\gamma^2 &\approx \frac{\lambda_o(1 + K_{uo}^2 + 2K_{uo}\Delta K_u\tau)\left(1 + \frac{\nu}{2\pi N}\right)}{2\lambda}
\end{aligned}$$

where higher order terms involving $(\Delta K_u\tau)^2$ and ν^2 have been dropped. Continuing with the approximation, equation (110.) can be written as

$$\gamma^2 \approx \frac{\lambda_o(1 + K_{uo}^2)}{2\lambda} \left[1 + \frac{2K_{uo}\Delta K_u\tau}{(1 + K_{uo}^2)} \right] \left[1 + \frac{\nu}{2\pi N} \right] \quad (111.)$$

Since the second term in each of the square brackets is assumed small, carrying out the multiplication yields

$$\gamma^2 \approx \frac{\lambda_o(1 + K_{uo}^2)}{2\lambda} \left[1 + \frac{2K_{uo}\Delta K_u\tau}{(1 + K_{uo}^2)} + \frac{\nu}{2\pi N} \right] \quad (112.)$$

At $\tau = 0$, $\gamma = \gamma_o$ and $\nu = \nu_o$, and equation (113.) becomes

$$\gamma_o^2 \approx \frac{\lambda_o(1 + K_{uo}^2)}{2\lambda} \left[1 + \frac{v_o}{2\pi N} \right] \quad (113.)$$

As the electrons travel down the undulator, both γ and v evolve in τ , and away from their initial values γ_o and v_o .

$$\gamma = \gamma_o + \Delta\gamma \quad (114.)$$

and

$$v = v_o + \Delta v \quad (115.)$$

Using equation (114.), equation (112.) becomes

$$\gamma^2 = \gamma_o^2 + 2\gamma_o\Delta\gamma + (\Delta\gamma)^2 \approx \frac{\lambda_o(1 + K_{uo}^2)}{2\lambda} \left[1 + \frac{2K_{uo}\Delta K_u\tau}{(1 + K_{uo}^2)} + \frac{v_o}{2\pi N} + \frac{\Delta v}{2\pi N} \right] \quad (116.)$$

For $N \gg 1$, $(\Delta\gamma)^2 \ll \gamma_o^2$, so the smaller term can be dropped from equation (116.). Using equation (113.) shows that γ_o^2 can be cancelled from both sides leaving

$$\gamma^2 = 2\gamma_o\Delta\gamma \approx \frac{\lambda_o(1 + K_{uo}^2)}{2\lambda} \left[\frac{2K_{uo}\Delta K_u\tau}{(1 + K_{uo}^2)} + \frac{\Delta v}{2\pi N} \right] \quad (117.)$$

Multiplying both sides by $1/2\gamma_o^2$ yields

$$\frac{\Delta\gamma}{\gamma_o} \approx \frac{\lambda_o(1 + K_{uo}^2)}{2\gamma_o^2\lambda} \left[\frac{K_{uo}\Delta K_u \tau}{(1 + K_{uo}^2)} + \frac{\Delta\nu}{4\pi N} \right] \quad (118.)$$

Now using equation (106.) to define the taper δ ,

$$\delta = -4\pi N \left(\frac{K_{uo}^2}{1 + K_{uo}^2} \right) \frac{\Delta K_u}{K_u} \quad (106.)$$

equation (118.) becomes

$$\frac{\Delta\gamma}{\gamma_o} \approx \frac{\lambda_o(1 + K_{uo}^2)}{2\gamma_o^2\lambda} \left[\frac{-\delta + \Delta\nu}{4\pi N} \right] \quad (119.)$$

Using the resonance condition equation (29.) with $\gamma = \gamma_R$, equation (119.) becomes

$$\frac{\Delta\gamma}{\gamma_o} \approx \frac{\gamma_R^2}{\gamma_o^2} \left[\frac{\Delta\nu - \delta}{4\pi N} \right] \quad (120.)$$

For $N \gg 1$, $\gamma_o \approx \gamma_R$, and equation (120.) simplifies to

$$\frac{\Delta\gamma}{\gamma_0} \approx \left[\frac{\Delta\nu - \delta}{4\pi N} \right] \quad (121.)$$

Equation (107.) can be written as

$$\eta = -\frac{\langle \Delta\gamma \rangle}{\gamma} = \frac{\delta - \langle \Delta\nu \rangle}{4\pi N} \quad (122.)$$

where $\Delta\nu = \nu_f - \nu_0$, therefore

$$\eta = \frac{\delta - \langle \nu_f \rangle + \langle \nu_0 \rangle}{4\pi N} \quad (123.)$$

where ν_f is the final electron energy, and ν_0 is the initial energy.

Equation (123.) holds for both positive, $\delta > 0$, and negative, $\delta < 0$, tapering, and examples of the change in efficiency for various taper values will be shown in the Chapter V.

THIS PAGE INTENTIONALLY LEFT BLANK

IV. TJNAF UPGRADE SIMULATIONS

In order to move from damage experiments with a laser spot size of a few millimeters to an actual weapon with a laser spot size of about 100 cm^2 , the average power of the laser must be increased. The current average power at the TJNAF FEL is 1.7 kW, and needs to be increased about 3 orders of magnitude to several megawatts for weapons applications.

At these higher MW power levels, energy efficiency becomes important. To operate more efficiently, the TJNAF FEL recirculates the electron beam after giving up energy to the light beam. The recirculated electrons are timed to arrive back at the entrance to the RF accelerator 180 degrees out of phase with the alternating electromagnetic field. This scheme has two advantages. First, it removes energy from the electrons so that they can be sent to a final beam dump without risk of producing neutron radiation. This requires the beam energy entering the dump to be less than 10 MeV. Second, the energy removed from the electrons can be used to boost the energy of the RF field. A diagram of the TJNAF FEL is shown in Figure 10.

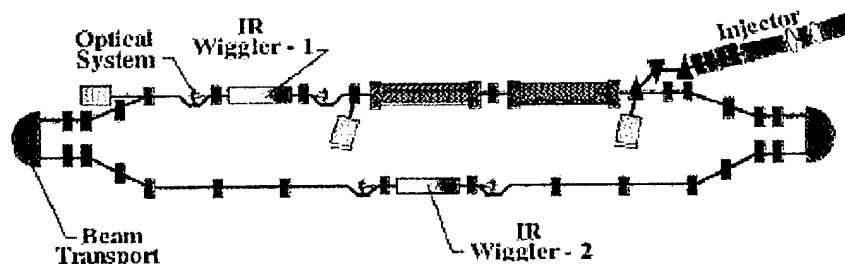


Figure 10. TJNAF FEL

Recirculation adds at least one new constraint to the FEL design. Since the electrons are being returned to the entrance to the accelerator, they must undergo turns totaling 360 degrees. The turns are accomplished through bending magnets. The electron's path through the turns is effected by its momentum, and by the magnetic force, which is proportional to the magnetic field and the velocity of the electron. The magnets are designed so that electrons moving through the turn at the correct speed will travel through the center of the beam pipe that makes up the turn. However, electrons with higher energy will be traveling faster than this design speed, and above a certain energy level their momentum will carry them into the outside wall of the turn, or to different points in the bending magnet field, or to different points at the entrance of the accelerator. Similarly, electrons with lower energy will

turn too quickly, and spread the beam. These effects place limits on the spread in energy that can be tolerated for a recirculated beam, and will have to be considered in the upgrade design.

As a first step in moving from 1.7 kW power to a megawatt class laser, TJNAF has decided to upgrade their current design to produce 10 to 20 kW average power. To support this goal, simulations were conducted to determine gain, power, and induced electron beam energy spread that would result from the design parameters chosen by the TJNAF personnel.

A. 20 KW SIMULATIONS

The first sets of simulations were for a 20 kW design and included simulations with and without a dispersive klystron undulator section. As shown in Figure 5 of Chapter III, an undulator can have a dispersive section that allows the electrons to continue transiting the optical cavity without any interaction. The effect of this dispersive section is to allow the electrons to use their slightly altered velocities from the first undulator section to bunch electrons prior to entering a second undulator section. This results in a significant increase in gain achieved in the second undulator section, but causes a reduction in

saturated power, as will be discussed in the following sections.

The design goals are to achieve 20kW of average power while maintaining a final energy spread of 6% or less to ensure that recirculation could take place. In order to improve gain in weak optical fields, TJNAF's 20kW design included a klystron undulator. The simulations varied the dispersive section strength D of this klystron undulator [Ref. 9], and varied desynchronism value d between the optical and electron pulse in order to compare gain, final power, and final electron energy spread. The parameters used in the simulations are shown in Table 4.

Table 4. 20 kW FEL Parameters.

PARAMETER	
Optical Wavelength λ	1.05 μm
Undulator Wavelength λ_0	20 cm
Peak Undulator Magnetic Field B	2 kG
Undulator Periods N	24
Undulator Length L	6 m
Undulator Parameter K	0.79
Dispersive Strength D	0, 1, 2 or 3
Electron Energy γmc^2	200 MeV
Electron Beam Radius r_b	0.5 mm
Electron Pulse Length l_e	2 ps
Initial Electron Phase Velocity Spread Standard Deviation σ_G	0.3
Electron Injection Angle Standard Deviation σ_θ	0.15
Peak Current I	200 A
Average Current	8 mA

Dimensionless Current Density j	2
Cavity losses ($Q = 10$)	10%
Peak Optical Power within cavity	40 GW
Repetition Rate	74.85 MHz
Duty Cycle	4×10^{-5}

1. Gain

Simulations were conducted for values of dispersive strength $D = 0, 1, 2$, and 3 , with $D=0$ representing the conventional undulator with no dispersive section. The desynchronism between electron pulse and optical pulse was also varied from $d = 0.0$ to 0.30 in steps of 0.02 .

The output from a typical simulation is shown in Figure 11. The variables used in this particular simulation are shown across the top of the figure and are: dimensionless current $j = 2$, the electron pulse length $\sigma_z = l_e / N\lambda = 2$,

angular electron velocity spread $\sigma_\theta = 4\pi N \frac{(\gamma^2 \Delta\theta^2)}{(1 + K^2)} = 0.15$

where $\Delta\theta$ is the electron beam angular spread, electron

phase velocity energy spread $\sigma_\epsilon = 4\pi N \frac{\Delta\gamma}{\gamma} = 0.3$, where $\frac{\Delta\gamma}{\gamma}$

is the fractional energy spread, desynchronism

$d = \Delta S / N\lambda = 0.03$, resonator cavity quality factor of $Q = 10^6$

to represent a cavity with practically no losses, undulator

periods $N = 24$, and dispersive section strength $D = 0$. The

high Q factor is chosen to determine the gain produced from

the beam interaction alone, ignoring any losses in the resonant cavity.

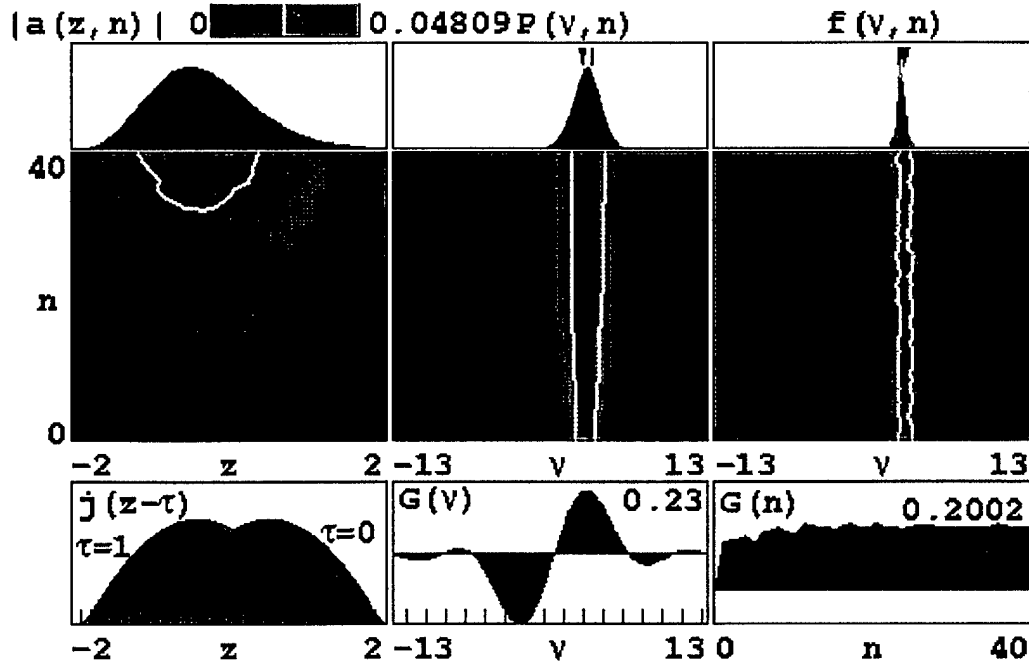


Figure 11. Simulation Results Showing Gain.

Figure 11 shows 9 sections arranged in a 3 x 3 grid pattern. The lower left corner indicates the position of the parabolic electron pulse shape. The electron pulse slips back by the slippage distance $N\lambda$ relative to the light pulse as both pulses move through the undulator from $\tau = 0$ to $\tau = 1$. The middle-left plot shows the evolution of the

optical field $|a(z, n)|$ as it grows over $n = 40$ passes through the undulator, with the final optical pulse shape shown in the top-left window.

The center graph shows the evolution of the optical power spectrum, $P(v)$ over $n = 40$ passes through the undulator. The top-center plot shows the final optical power spectrum after $n = 40$ passes. The bottom-middle plot is the weak-field gain spectrum, $G(v)$, showing a maximum gain occurring at $v = 2.6$.

The lower-right window shows the gain of the optical pulse $G(n)$. The middle-right plot shows the evolution of the electron spectrum $f(v)$ over $n = 40$ passes, while the top-right plot shows the final spectrum after $n = 40$ passes through the undulator.

The gain results from many simulations at different values of desynchronism d is plotted in Figure 12. The conventional undulator with $D = 0$ achieved a maximum gain of $G = 0.2$ at a desynchronism value $d = 0.03$. The maximum gain of $G = 0.67$ was achieved for the klystron undulator with dispersive strength $D = 2$. This was 3 times higher than the gain of the conventional undulator with $D = 0$. However, the higher gain achieved using a klystron undulator comes at the expense of a lower power at saturation, as described in the next section.

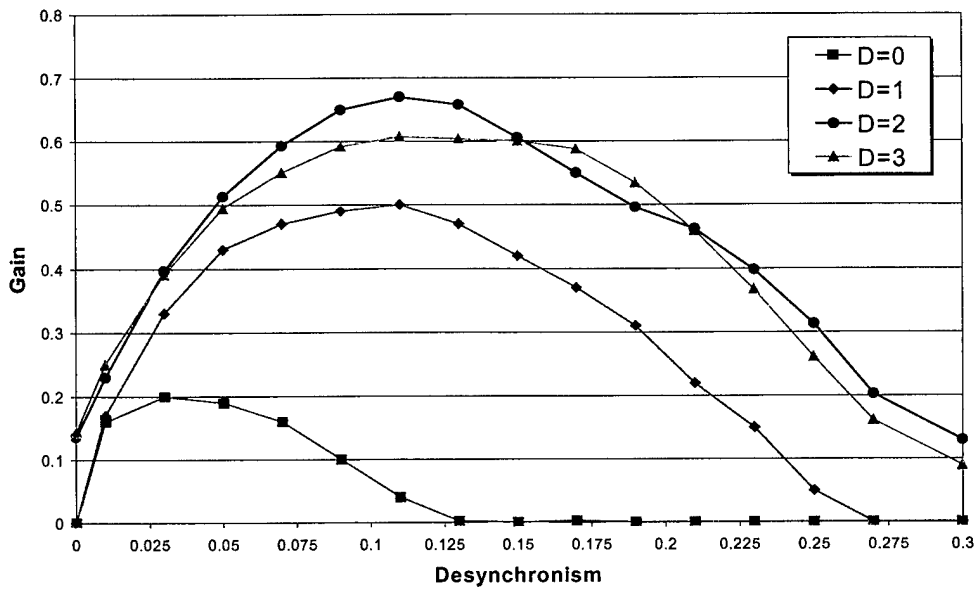


Figure 12. Steady State Gains

2. Power

A typical output showing the power evolution of the optical beam is shown in Figure 13. All the variables used in this simulation were the same as used in the gain simulation of Figure 11, except that the simulation has been allowed to run to $n = 1200$ passes, and the quality factor has been reduced to $Q = 10$. This Q represents the actual TJNAF FEL cavity loss of $1/Q = 10\%$. In Figure 13, the optical power as a function of n passes is plotted in the lower-right corner, while all the other windows of the plot remain the same as described in Figure 11.

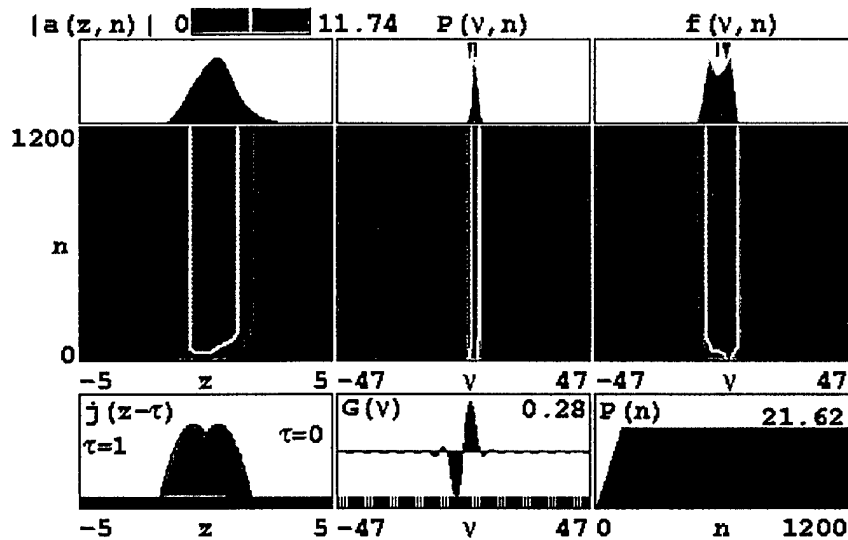


Figure 13. Simulation Results for Conventional Undulator.

Figure 14 shows the results of many simulations plotting the final average power as a function of dispersive strength D and desynchronism value d . Maximum power was achieved with the conventional undulator and dispersive strength $D = 0$. The power level achieved was 14 times higher than the closest klystron undulator which used dispersive strength $D = 1$. Klystrons with dispersive strengths $D = 2$ and $D = 3$ resulted in even lower power levels.

The results shown in Figure 14 seem to indicate that the conventional undulator is the obvious design to choose

in order to achieve maximum power. However, strong fields in the conventional undulator cause the trapped-particle instability. This causes the electron beam energy spread to move outside the 6% design tolerance.

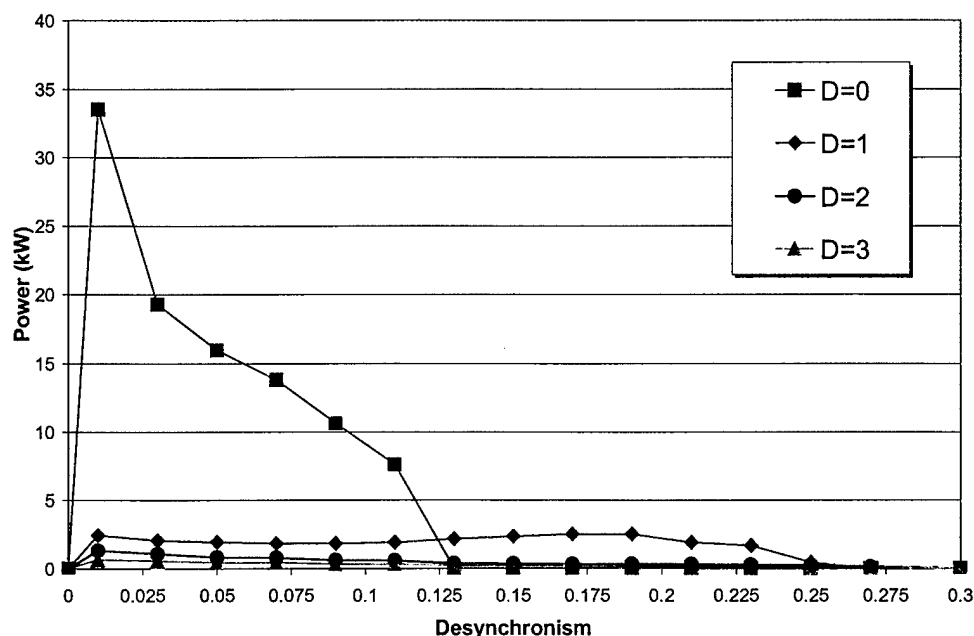


Figure 14. Final Power vs. Desynchronism

3. Energy Spread

Figure 15 shows the final induced electron beam energy spread produced by the 4 different undulators for desynchronism values $d = 0.0$ to 0.15 . As can be seen in this figure, the conventional undulator with $D = 0$ has a peak energy spread of 8.6% occurring at $d = 0.007$. The

energy spread decreases with increasing desynchronism, and falls below the desired 6% level at a desynchronism value of $d = 0.06$, and remains below 6% for all larger values of d .

For the klystron undulator with dispersive strength $D = 1$, the maximum energy spread is 5%, which occurs at desynchronism values from $d = 0.01$ to 0.06 . It also shows a decrease in the energy spread with an increase in desynchronism above $d = 0.06$. The klystrons with $D = 2$ and $D = 3$ have an energy spread of about 2% for all values of desynchronism.

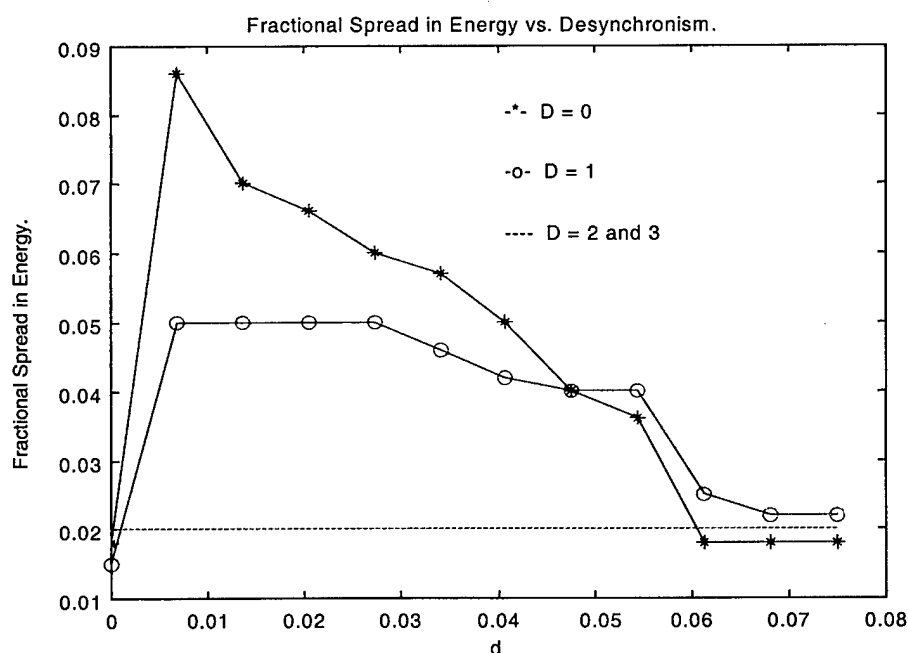


Figure 15. Energy Spread vs. Desynchronism

4. Conclusions of 20kW Simulations

As expected, the maximum gain was achieved with a klystron undulator. Using a klystron undulator with dispersive strength $D = 2$ produced a steady state gain of 67%. However, this increased gain leads to a tremendous reduction in final power. The $D = 2$ klystron design's final power was approximately 15 times smaller than that of the conventional undulator.

The conventional undulator achieved the highest final power, which occurred at a desynchronism of $d = 0.007$. However, at this desynchronism, the induced energy spread was 8.6%, which is outside the limits imposed by recirculation. Increasing the desynchronism to $d = 0.03$ reduces the energy spread down to the desired 6%, while achieving a final output power that is still 9 times higher than the best klystron undulator design. Simulations using a conventional undulator with a desynchronism value of $d = 0.03$ produced a final power of 19.2 kW, which is close to the 20kW objective, and corresponds to a final gain of 19%.

Results for the 20 kW simulations were presented at the 20th International Free Electron Conference in Williamsburg, VA, and were published in Nuclear Instruments and Measurements. [Ref. 9]

B. 10 KW SIMULATIONS

Recently, simulations for a 10 kW upgrade design were conducted. The design parameters are listed in Table 5.

Table 5. 10 kW FEL Parameters

PARAMETER	
Optical Wavelength λ	5.8 μm
Undulator Wavelength λ_o	20 cm
Undulator Periods N	24
Undulator Length L	4.8 m
Undulator Parameter K	1, 2, 3, or 4
Dispersive Strength D	0, 0.25, 0.5, 0.75 or 1
Electron Energy γmc^2	150 MeV
Electron Beam Radius r_b	0.35 mm
Electron Pulse Length σ_z	0.5 ps
Initial Electron Phase Velocity Spread Standard Deviation σ_G	0.5
Peak Current I	270 A
Average Current	10 mA
Dimensionless Current Density j	2.9 - 3.7
Cavity losses	15%
Peak Optical Power within cavity	1.5 MW
Repetition Rate	74.85 MHz
Duty Cycle	3.75×10^{-5}

In addition to conducting simulations for various values of dispersive strength and desynchronism, these simulations also varied the value of the undulator parameter K from 1 to 4 in steps of unity. Table 6 shows the parameters affected when the undulator parameter is varied:

λ = the optical wavelength, σ_z = the dimensionless pulse length, j is the dimensionless current density, and F is the filling factor which is the ratio of the area of the electron beam to the area of the optical beam averaged over the interaction region.

Table 6. Dimensionless Variables vs. K.

	K=1	K=2	K=3	K=4
λ	2.3 μm	5.8 μm	12 μm	20 μm
σ_z	2.7	1.1	0.54	0.32
jF	2.9	3.7	3.8	3.8
F	0.06	0.02	0.01	7×10^{-3}

1. Power

Simulations were carried out for desynchronism values d ranging from 0 to 0.3. The dispersive strengths for these simulations were varied from $D = 0.0$ to $D = 1.0$ in steps of 0.25. Figure 16 shows the output for the conventional undulator design $D = 0$, desynchronism $d = 0.025$, and undulator parameter $K = 2$.

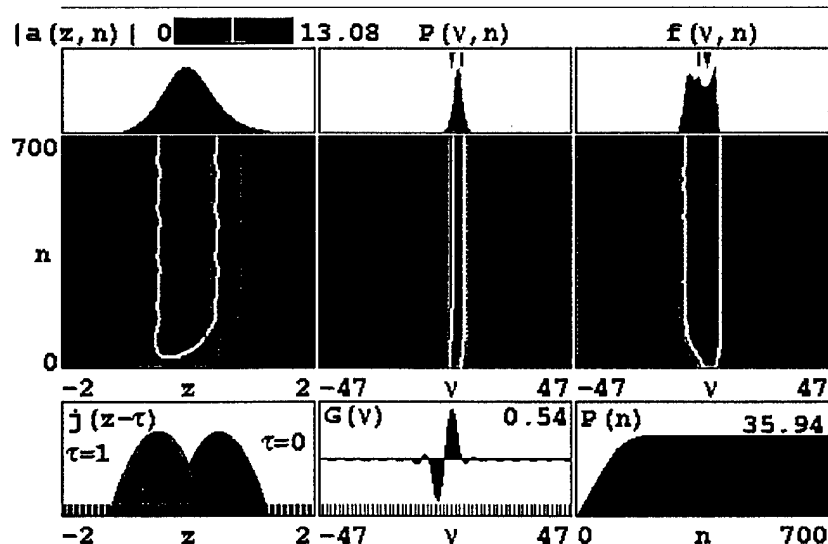


Figure 16. Power Simulation for Klystron Undulator

Figure 17 shows the maximum power achieved for various values of K and $D = 0$ (no klystron). The maximum power was achieved for the $K = 2$ undulator parameter, with a final power of 14.5 kW. This was also the maximum power achieved out of all 360 simulations conducted for the various undulator parameters K , dispersive strengths D , and desynchronism values d . Figure 17 also shows that the $K = 1$ simulations achieved similar final power levels at varying desynchronism values. The energy spread for these simulations was approximately 5.5%, which was within the 6% specification for recirculation. No power is achieved for the $K = 3$ and 4 simulations due to the smaller filling

factor F and the shorter dimensionless electron pulse length σ_z . Note that the actual electron pulse length l_e remains fixed, but the slippage distance $N\lambda$ is larger.

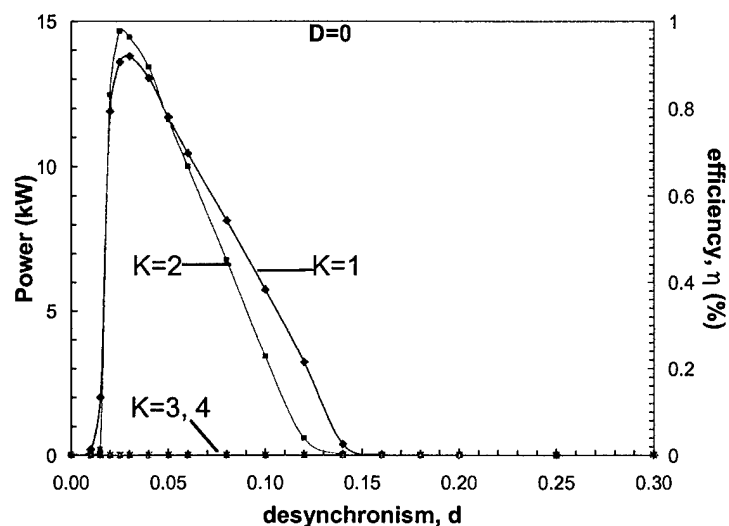


Figure 17. Final Power, Conventional Undulator

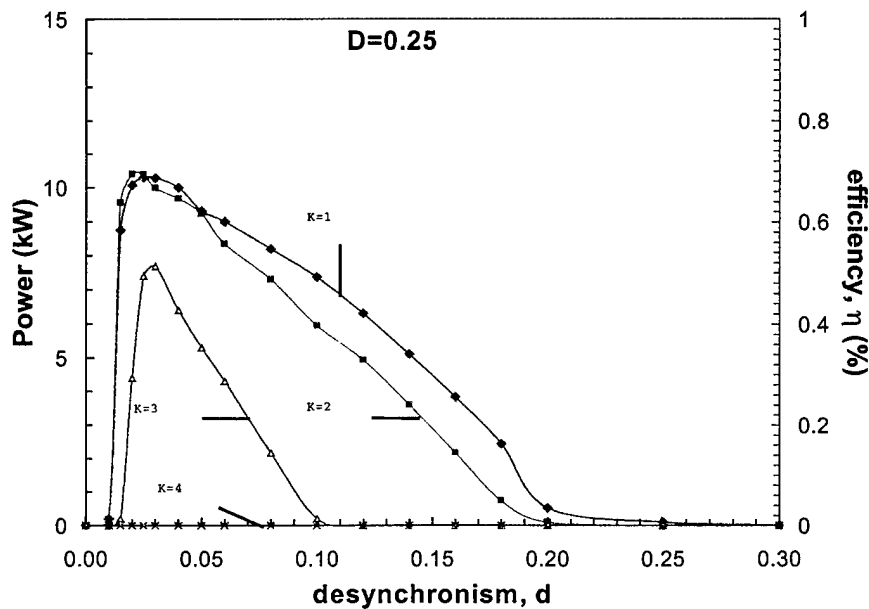


Figure 18. Final Power, Weak Klystron Undulator

Figure 18 shows the final power after introduction of a weak klystron of $D = 0.25$. The figure shows that the klystron has added enough gain to produce power for the $K = 3$ simulations, but at a final power level of only 7.5 kW. The maximum power achieved using the $K = 1$ and 2 values has dropped from 14.5 kW to approximately 10 kW. The energy spread for these simulations was reduced to about 4% because of the lower power.

With stronger klystron values of $D = 0.5$ and up to $D = 1$, all four undulator parameter values produced some output power, but less than the desired 10 kW. The maximum average

power achieved for the higher D values was for $K = 3$, $D = 0.50$, which produced a peak power of 6.7 kW.

2. 10 kW Simulation Conclusions

From the 360 simulations conducted for the 10 kW design, it appears that the conventional undulator $D = 0$, and the weak klystron undulator with $D = 0.25$, will meet the desired goals. However, both undulator designs have marginal areas of operation. For the weak klystron undulator of $D = 0.25$, the energy spread was very good at 4%, but the final output power was only slightly higher than the desired 10 kW. For the $D = 0$ undulator (no klystron), the output power was much higher at 14.5 kW, but the energy spread was about 5.5%, which is close to the 6% limit.

Results for the 10 kW simulations were presented at the 22nd International Free Electron Laser Conference in Raleigh, NC, and will be published in Nuclear Instruments and Measurements. [Ref. 7]

V. TAPERING

It is only near resonance that the coupling between the laser and electron beams is significant. As the electrons lose energy to the light beam, they move away from resonance. In order to maintain or re-establish the resonance condition, the undulator properties can be tapered so that as the electrons lose energy, the resonant energy also decreases. The theory of tapering by either changing the undulator wavelength λ_0 , or changing the undulator magnetic field strength is discussed in section F of Chapter III.

Without tapering, the electrons begin to bunch early in the growing optical field, and eventually move to points in phase space where they are no longer losing energy but are gaining energy from the light beam. When the optical field reaches this level the FEL is said to have reached saturation. The tapered undulator increases gain and efficiency in strong optical fields and extends the usual saturation limit to stronger optical fields by maintaining the resonance condition. As electrons lose energy γmc^2 , the resonance condition, $\lambda = \lambda_0 \frac{(1+K^2)}{2\gamma^2}$, would indicate that

either reducing the undulator wavelength, λ_0 , or the undulator parameter, K , would restore resonance.

Since the purpose of tapering is to reduce the resonance energy to match the reduced energy of the electrons, it would seem that there would be no benefit in using an inverse taper where the undulator wavelength, λ_0 , is increased, or the undulator magnetic field strength, K , is increased. However, simulations show that there are several possible advantages to using the inverse taper.

The electron dynamics in a tapered undulator were described by equation (102.) of chapter III as

$$\ddot{\zeta} = \delta + |a| \cos(\zeta + \phi) \quad (102.)$$

where ζ is the electrons phase in the ponderomotive wave, ϕ is the optical phase, $a = |a|e^{i\phi}$ is the complex dimensionless optical field strength, and δ is the acceleration torque term resulting from tapering. Simulations using both positive and negative values of δ , corresponding to positive and negative taper of K or λ_0 , were carried out and the results will be discussed in following sections.

A. EFFICIENCY AND ENERGY SPREAD

When designing a high power recirculating free electron laser, both efficiency and induced energy spread are important. As defined in equation (107.) of Chapter III, efficiency η is

$$\eta = - \frac{\langle \Delta \gamma \rangle}{\gamma_0} \quad (107.)$$

and is typically highest in strong fields. However, strong fields have the adverse effect of inducing a larger electron energy spread along the undulator. For our purposes, energy spread is defined as the full spread in phase velocity,

$$V_s = V_{\max} - V_{\min} \quad (124.)$$

The difficulty for a recirculating FEL operating in strong fields arises because some electrons gain energy while some lose energy. This makes the spread in energy large but does not necessarily make the efficiency large.

A second difficulty arises when considering high power FELs. The small percentage of electrons that may lie in the outer tails of the energy distribution cannot be ignored, because for high power FELs these tails represent a lot of current. When recirculating high current (for high power),

this small fraction of the electron beam in distribution can cause serious damage to the vacuum beam pipe, as well as radiation problems as the electrons collide with the walls of the recirculating path. Consider just 0.01% of a 1A (average current) beam at 100 MeV energy focussed to a 1 mm^2 spot; the irradiance is 1 MW/cm^2 . The damage would occur rapidly. Therefore, when discussing energy spread for high current recirculating devices, the electrons in the tails of the distribution must be included as in equation (124.).

B. NO TAPER

In the conventional undulator with weak initial optical field $a_0 < \pi$, the gain spectrum is shown in Figure 19. It is symmetric about resonance with a peak gain of 27% for $j = 2$, occurring at an initial phase velocity $v_0 = 2.6$. The gain spectrum width is $v_s \approx \pi$, and the gain is zero at resonance $v_0 = 0$.

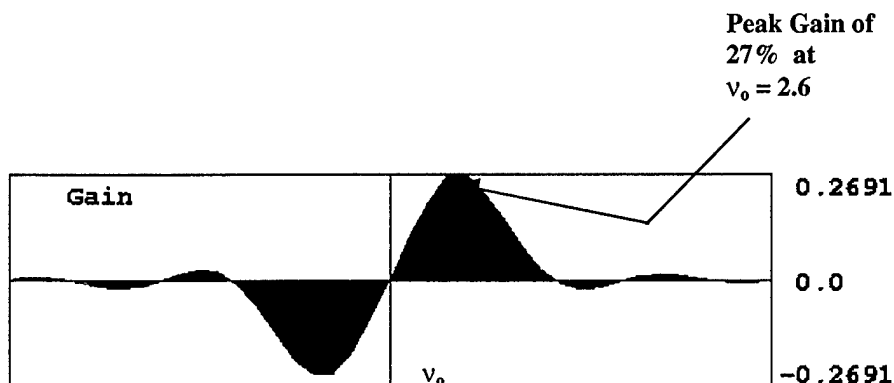


Figure 19. Weak Field Gain Spectrum

As the optical field grows, the gain spectrum changes in shape. Figure 20 shows the spectrum as the optical field grows from $a_0 = \text{small}$ to saturation at $a_0 = 40$.

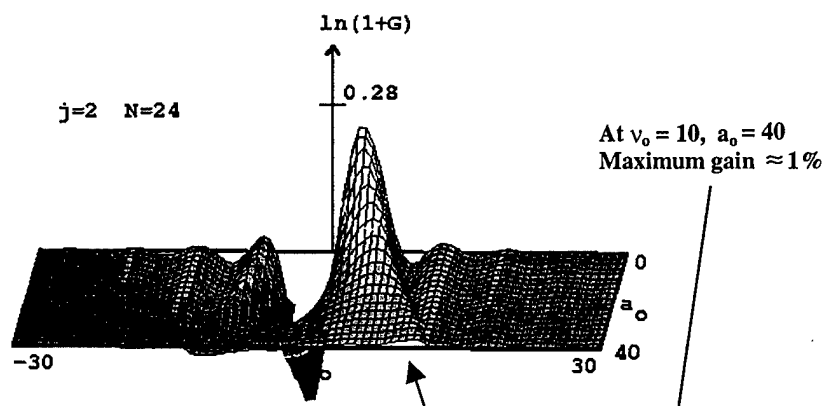


Figure 20. Gain vs. v_0 in Increasing Optical Field a_0

The spectrum is still symmetric about resonance, but the peak gain has been reduced to approximately 1% at an initial phase velocity of $v_0 = 10$. At saturation, the FEL

oscillator wavelength will shift to follow the point of maximum gain, and in this case will shift from $\nu_0 = 2.6$ to $\nu_0 = 10$, which corresponds to a shift of about 5% in optical wavelength for $N = 25$.

In the electron pendulum phase-space determined by Equation (102.), saturation in strong fields occurs when electrons become trapped in closed orbits as shown in Figure 21.

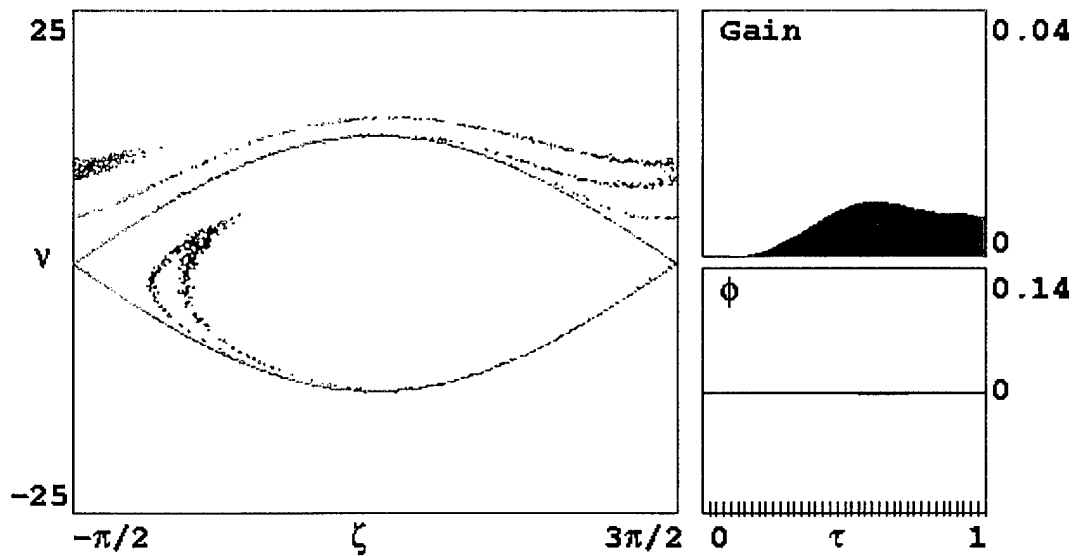


Figure 21. Phase Space for Conventional Undulator.

When the pendulum separatrix height, $4\sqrt{a}$, becomes greater than the phase velocity for peak gain in weak fields, $v_0 = 2.6$, an increasingly larger fraction of the electron beam becomes trapped in the closed orbit region of phase space. At saturation, the FEL interaction induces a spread in phase velocities which is slightly larger than the height of the separatrix, $v_s \approx 4\sqrt{a} \approx 8\pi$, or about 10% for $N = 25$. This spread is sufficient to effect the recirculation of the electron beam.

C. POSITIVE TAPERING

When someone speaks of tapering the undulator, they usually mean positive tapering: either the undulator period λ_0 is decreased along the undulator, or the magnetic field strength is decreased along the undulator, or both. With a modest taper, the maximum weak field gain is shifted and occurs at initial phase velocity $v_0 \approx 2.6 - \delta/2$. As can be seen by comparing Figure 20 with Figure 22, the weak-field gain is reduced for a tapered undulator. However, strong field gain is increased. For a taper of 6π , the weak field maximum gain is shifted to $v_0 \approx -7$. In strong fields of $a_0 = 40$, the gain spectrum has become flattened and distorted, and the maximum gain has shifted to $v_0 \approx 0$. In

strong fields the gain has increased from $G \approx 1\%$ in the untapered undulator, to $G \approx 2\%$ with taper.

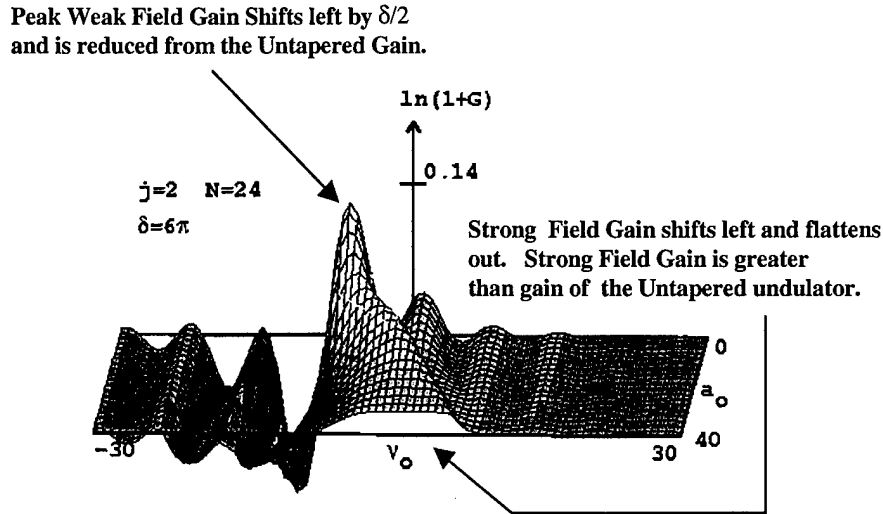


Figure 22. Gain vs. v_0 in Increasing Optical Field a_0 for a Tapered Undulator.

The separatrix surrounding the closed-orbit paths in phase space is given by [Ref. 29, pg. 157]

$$v_s^2 = 2\delta(\zeta_s - \zeta_o) + 2a(\sin(\zeta_s) - \sin(\zeta_o)) \quad (125.)$$

where

$$\zeta_o = 2\pi - \cos^{-1}(-\delta/|a|) \quad (126.)$$

In the tapered undulator, the phase paths are modified by the acceleration term δ in the pendulum equation. For $\delta > a$, the \cos^{-1} expression has no solution, and there is no separatrix surrounding closed orbit paths.

The change in the separatrix can be calculated starting with equation (125.). With a tapered undulator, the separatrix height is reduced, and has been shown by Massey [Ref. 30] to be

$$h = 4\sqrt{a} \left(\sqrt{|q|} \cos^{-1}(-|q|) + \sqrt{1-q^2} \right) \quad (127.)$$

where $q = \delta/a$. When the taper is too large, such that $\delta > a$, the electrons phase space has no closed orbits.

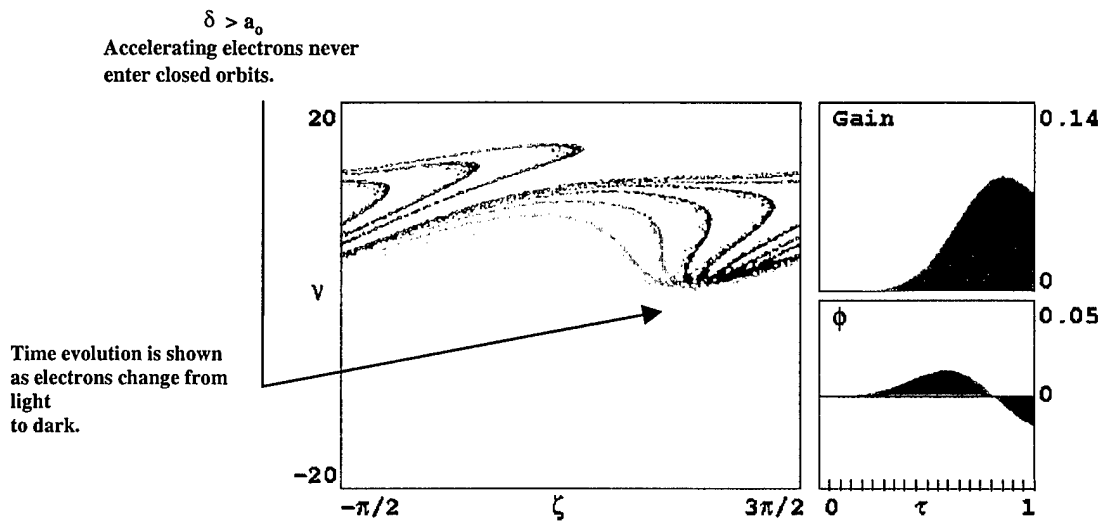


Figure 23. Phase Space Showing $\delta > a_0$.

In sufficiently strong fields, $a_0 > \delta$, some of the electrons can be trapped in the closed orbits of the pendulum phase space. This is illustrated in Figure 24. In stronger fields, $a_0 \gg \delta$, a large fraction of the electrons can be trapped near resonance around $\zeta \approx \pi$, and continue to lose energy to the optical field, as is illustrated in Figure 25.

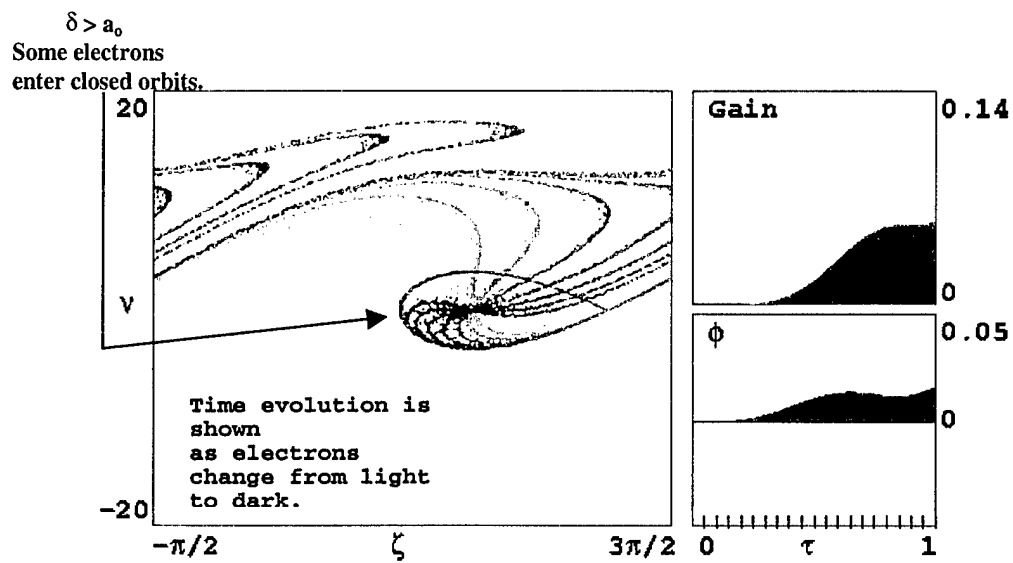


Figure 24. Phase Space Showing $a_0 > \delta$.

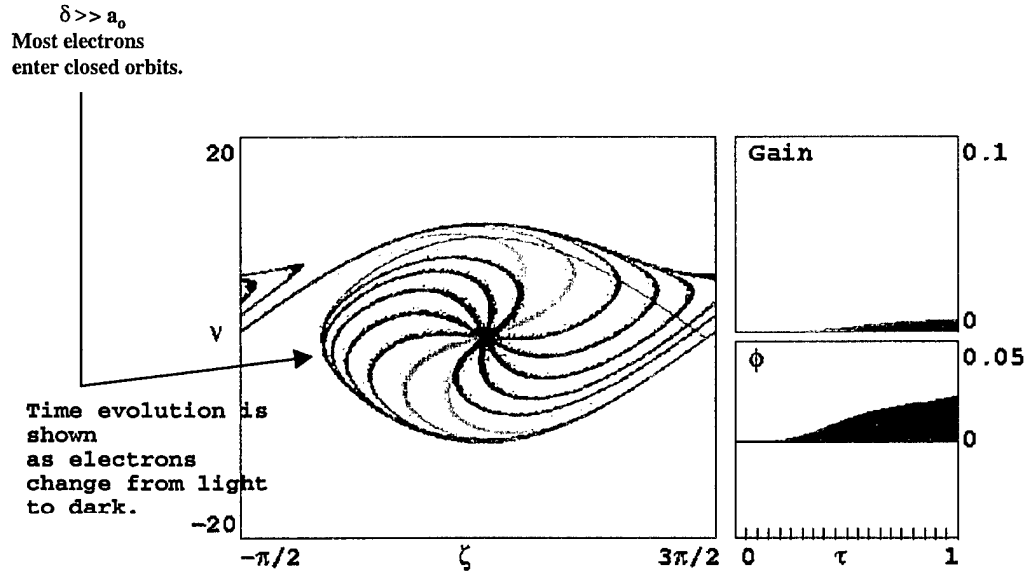


Figure 25. Phase Space Showing $a_0 \gg \delta$.

As shown in Figure 26 below, electrons starting near the phase $\zeta \approx 0$ are accelerated by both the torque δ and the strong optical field a , while the electrons starting near $\zeta \approx \pi$ see the acceleration term δ and a roughly cancel, leaving them trapped in closed orbits. Tapering is effective because the electrons near the maximum gain point of $\zeta \approx \pi$ are trapped, while the electrons near the phase point for absorption $\zeta \approx 0$, are taken away from resonance and eventually stop interacting. It is this imbalance between the gain and loss mechanisms that leads to gain.

Torque term δ and optical field a_0 add together for electrons starting near $\zeta_0 = 0$.

Torque term δ and optical field a_0 cancel together for electrons starting near $\zeta_0 = \pi$.

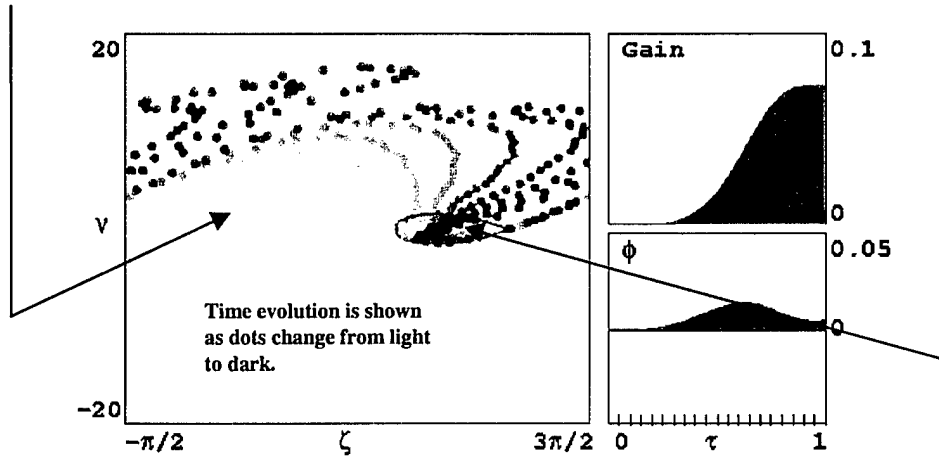


Figure 26. Separatrix for Positive Tapered Undulator.

As can be seen in Figure 27, which shows only the final position of each electron, the electrons appear to have an energy spread with about half of the electrons trapped near resonance $\nu \approx 0$, and the other half untrapped at $\nu \approx \delta + 2\sqrt{a}$. In a strong field of $a = 40$ and with a taper rate of $\delta = 5\pi$, the induced spread approximately $\nu_s \approx \delta + 2\sqrt{a} \approx 15 + 2\sqrt{40} \approx 30$. Due to this large energy spread, the tapered undulator does not appear to be desirable for recirculating the electron beam.

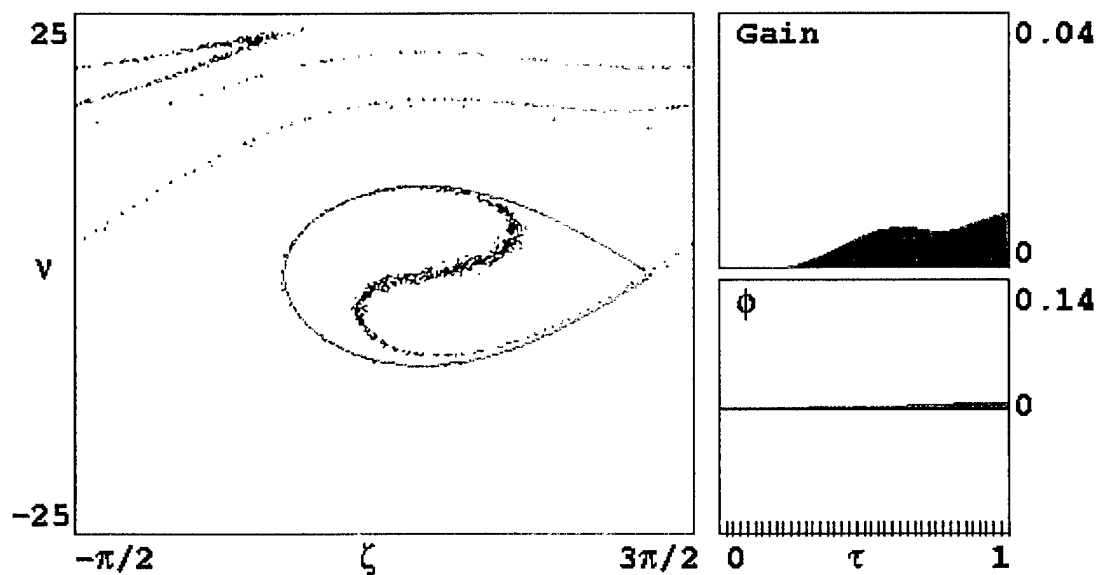


Figure 27. Phase Space for Positive Tapered Undulator.

D. NEGATIVE TAPER

In the negative or inverse tapered undulator, the acceleration term $\delta < 0$. Initial investigations and simulations into the use of negative taper indicated some favorable results could be obtained in the areas of strong field gain and energy spread.

Figure 28 shows the gain spectrum for an FEL with inverse taper rate $\delta = -6\pi$ over $N = 24$ periods with a current density of $j = 2$. These parameters are descriptive

of the TJNAF FEL with recirculation of the electron beam. In weak fields, $a \leq \pi$, the gain spectrum peak is shifted above resonance to $\nu_0 \approx 2.6 - \frac{\delta}{2} \approx 12$, with a peak gain of $G = 12\%$. This gain is comparable to the positive taper case shown previously in Figure 22 above. Both positive and negative taper have the effect of shifting the gain spectrum by $\nu_0 \approx 2.6 - \frac{\delta}{2}$, and reducing the peak gain available by about 50% when $\delta = \pm 6\pi$.

In stronger fields, the gain spectrum distorts and flattens, but in a manner that differs from both the non-tapered and positive tapered undulators. As shown in Figure 28, the peak in the gain spectrum tends to stay near the same value ν_0 with only a slight shift from $\nu_0 = 12$ to $\nu_0 = 13.5$ as the field grows from weak to strong values. This means that in a FEL with inverse taper, the expected wavelength shifts only slightly as the laser approaches saturation. The peak gain in strong fields does decrease, but only down to 3%, which provides a significant advantage over the untapered undulator, and even betters the positive tapered undulator. This result was unexpected since the tapered undulator has long been thought to provide the best extension of the FEL to strong fields.

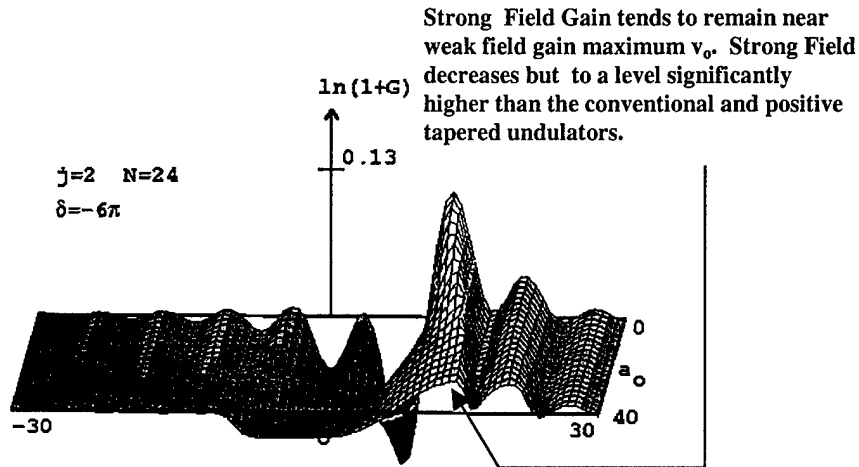


**Figure 28. Gain vs. v_0 in Increasing Optical Field a_0
 for a Inversely Tapered Undulator.**

The electron evolution in phase space with inverse taper is also quite different than the other two undulator types. The separatrix shown in Figure 29 is still given by equation (124.) above, but with $\delta < 0$. Figure 29 is shown for a taper rate of $\delta = -6\pi$, $N = 24$ periods, and a current density of $j = 2$.

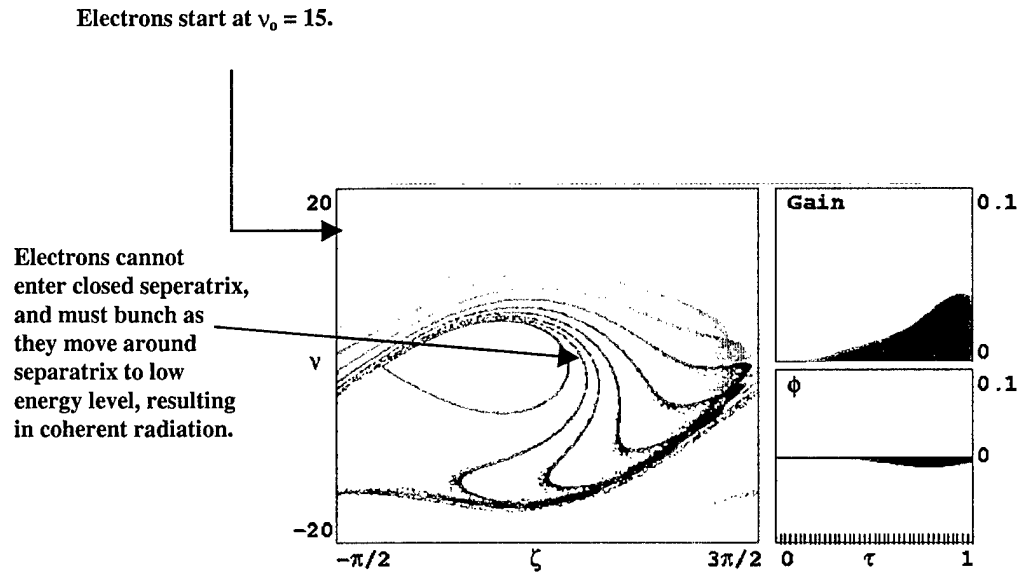


Figure 29. Phase Space for an Inverse Tapered Undulator.

The electrons started at $v_0 = 15$, which provides the peak gain in strong fields for this taper. All of the electrons start in open phase space paths far from resonance and cannot enter the closed-orbit region inside the separatrix. Following the open-orbit paths, it is clear that the electrons must bunch as they lose energy to travel around the closed-orbit region. The bunch continues to follow open orbit paths down to a final phase-space site around $v \approx -20$ where they have lost considerable energy. More importantly, the induced average energy spread in the final electron distribution appears to be relatively small. Most of the final electrons are located in a spread of $v_s \approx 15$ around $v = -16$, with a tail extending back to

resonance. This corresponds to only a 4% average energy spread. This is significantly reduced compared to the tapered undulator spread of 13% and the periodic undulator spread of 10%.

These results are surprising and appear promising for a recirculating FEL. For high power recirculating FELs, it is the full energy spread that is important. The electrons at the extreme edges of the distribution must be considered. Figure 30 provides a phase space view of a undulator with a taper of $\delta = -5\pi$, showing only the final position of the electrons. Most of the electrons are bunched around $\nu = -20$, there are still some electrons at the top of the separatrix around $\nu = 8$. When considering the full spread of electrons, a comparison of Figure 21 and Figure 27 with that of Figure 30 shows that the inverse tapered undulator's full spread is $\nu_s \approx 28$. This is only a modest improvement over the untapered and positive tapered undulator with a full spread of $\nu_s \approx 30$.

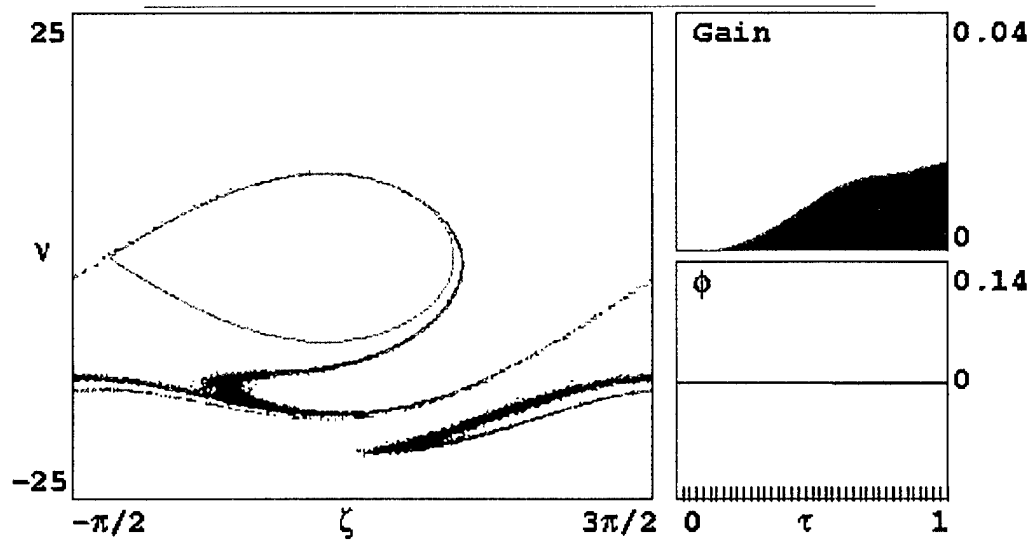


Figure 30. Phase Space for a Negative Tapered Undulator.

E. CONCLUSIONS OF THE CONVENTIONAL AND TAPERED UNDULATORS

The inverse tapered undulator appears to offer advantages over both the periodic and tapered undulators. The advantages include larger gain in strong fields, smaller wavelength shift at saturation, and a smaller induced average energy spread.

The increase in gain over the untapered undulator in strong fields appears to be about 3 to 1, while the increase

in gain over the negative tapered undulator is about 1.5 to 1.

While both the untapered and positive tapered undulators have large shifts in resonant wavelength as the optical field grows to saturation, the inversely tapered undulator experiences only a minor shift. The result for inverse taper is only a slight shift in the lasing wavelength as the optical field grows from start-up to saturation.

The induced full width half maximum energy spread is greatly reduced for the inverse tapered undulator. However, the full width energy spread is only slightly improved by using the inverse taper design.

Initial results from the inverse taper simulations were presented at the 21st International Free Electron Laser conference, and published in Nuclear Instruments and Measurements. [Ref. 8] Additional results were presented at the 22nd International Free Electron Laser conference, and will be published in Ref. 7.

LIST OF SYMBOLS

a	Dimensionless optical field
\dot{a}	Dimensionless derivative of optical field
a_0	Dimensionless optical field at start of undulator
A	Area
$B_{x,y,z}$	Magnetic Field in x, y, or z direction
B_u	Undulator Magnetic Field
β	Fractional speed (velocity/speed of light)
c	Speed of light in vacuum
C	Specific Heat
d	desynchronism value
D	Dispersive strength
D_L	Thermal Diffusion length
δ	Dimensionless taper
δ^3	Three dimensional Dirac delta function
e	Electron charge
E	Energy
E_s	Electric Field
ϵ	Unit vector symbol
F	Filling factor
Φ	Irradiance or Flux density
Φ_0	Required Flux Density
ϕ	Initial phase of optical wave

G	Optical field gain
γ	Lorentz factor
γ_0	Initial Lorentz factor
γ_R	Resonance condition Lorentz factor
ΔH_m	Latent heat of melting
ΔH_v	Latent heat of vaporization
η	Efficiency
j	Dimensionless current
J	Current
k	Optical wave vector
k_0	Undulator wave vector
K	Thermal conductivity
K_u	Undulator parameter
κ	Thermal diffusivity
L	Length
λ	Optical wavelength
λ_0	Undulator wavelength
m	Mass
n	Number of passes through the undulator
N	Undulator Periods
v	Phase velocity
v_f	Final Phase velocity

v_o	Initial Phase velocity
v_s	Energy Spread
P	Power
Q	Resonator quality factor
r_i	Distance in the 'i' direction
R	Radius
R_{ih}	Radius of the hole for the ' i^{th} ' run
R_{it}	Radius of the entire damaged area for the ' i^{th} ' run
ρ	Mass density
ρ_e	Electron density
S	Resonator cavity length
σ_g	Electron phase velocity spread
σ_θ	Electron angular spread
σ_z	Electron pulse length
T	Temperature
T_m	Melting temperature
T_o	Initial temperature
T_v	Vaporization temperature
T_p	Pulse length
τ	Dimensionless variable for length
v	velocity
V	Volume
V_{ih}	Volume of the hole for the ' i^{th} ' run
V_{it}	Volume of the entire damaged area for the ' i^{th} ' run

ω	Radian frequency
Ψ	Phase of optical wave
y	Thickness of material
z	Depth of hole
ζ	Electron Phase

LIST OF REFERENCES

1. "...From the Sea: Preparing the Naval Service for the 21st century", NavNews 048/92, Article NNS 130, 6 October 1992.
2. "Forward...From the Sea: The Navy Operational Concept", March 1997.
3. "Navy Strategic Planning Guidance with Long Range Planning Objectives.", Office of the Chief of Naval Operations, April 2000.
4. Hamilton, G.K., "Surface Warfare Magazine", March/April 1999, pgs 2 - 7.
5. "Janes Fighting Ships 2000-2001, Janes Information Group Unlimited, Sentinel House, Coulsdon, Surrey, UK.
6. "Technology for the United States and the Marine Corps, 2000 - 2035. Becoming a 21st-Century Force.", Vol. 5., Naval Studies Board, Commission on Physical Sciences, Mathematics, and Applications, National Research Council, National Academy Press, 1997.
7. McGinnis, R.D., Blau, J., Colson, W.B., Massey, D., Crooker, P.P., Christodoulou, A., Lampiris, D., "Proceedings of the 22nd International Free Electron Laser Conference", Nuclear Instruments and Measurements, North Holland, Elsevier, Amsterdam. 2000
8. Colson, W.B. and McGinnis, R.D., "Proceedings of the 21st International Free Electron Laser Conference", Nuclear Instruments and Measurements, North Holland, Elsevier, Amsterdam, 1999.
9. LeGear, R.E., Steele, R.B., McGinnis, R.D., Colson, W.B., "Proceedings of the 20th International Free Electron Laser Conference", Nuclear Instruments and Measurements, North Holland, Elsevier, Amsterdam, 1998.
10. Cook, J.R. and Albertine, J.R., "High Energy Laser Weapon systems," Surface Warfare, Sept/Oct 1997, Vol. 22, No. 5.

11. Von Allmen, M. "Laser-Beam Interactions with Materials"., Springer-Verlag, Berlin, Germany., 1987.
12. Cozzens, R.F., "Missile Radome Materials, Vulnerability to High Energy Laser Radiation", Naval Research Laboratory, 1996.
13. Kittel, C. "Introduction to Solid State Physics", 5th Edition, John Wiley and Sons, 1976.
14. Woehler, K.E., PH 4054 Course Notes, Naval Postgraduate School, 1998
15. Anderberg, B., MGEN, and Wolbarsht, M.L., "Laser Weapons: The Dawn of a New Military Age", Phenum Press, New York, NY. 1992.
16. Schriempf, J.T., "Response of Materials to Laser Radiation: A Short Course", Naval Research Laboratory, Washington, D.C., July 1979.
17. Ang, L.K., Lau, Y.Y., Gilgenbach, R.M., Spindler, H.L., Lash, J.S., Kovaleski, S.D., "Surface Instability of Multipulse Laser Ablation on a metallic target", Journal of Applied Physics, April, 1998, Vol. 83, No.8.
18. Anisimov, S.I., et al., "Electron Emission from Metal Surfaces Exposed to Ultrashort Laser Pulses", Sov. Phys. JETP, August 1974, Vol. 39, No. 2.
19. Corkum, P.B., Brunel, F., Sherman, N.K., Srinivasan-Ran., T., "Thermal Response of Metals to Ultrashort-Pulse Laser Excitation", Physical Review Letters., December 1988, Vol. 61, No 25.
20. Stuart, B.C., Feit, M.D., Herman.S., Rubenchik, A.M., Shore,B.W., Perry, M.D., "Nanosecond to Femtosecond Laser Induced Breakdown in Dielectrics", Physical Review Letters, Vol. 53., No. 4., January, 1996.
21. Du, D., Liu, X., Korn, G., Squier, J., Mourou, G., "Laser-induced Breakdown by Impact Ionization in SiO₂ with Pulse Widths from 7 ns to 150 fs", Applied Physics Letters, June 1994, Vol. 64. No. 3.
22. Shinn, M.D., Personal Communication, Letter dated 13 May 1999.
23. Powell, J.B., CAPT, USN, Personal Communications of 18 October, 2000.

24. Wenzel, D., Naval Research Laboratory, Personal Communication, Electronic Mail, 16 March 1999.
25. McGinnis, R.D., Thomson, R.W., Short, L.R., Herbert, P.A., Lampiris, D., Christodoulou, A., Colson, W.B., Shinn, M.D., Neil, G., Benson, S., Gubeli, J., Evans, R., Jordan, K., "Free Electron Laser Material Damage Studies", Naval Postgraduate School Technical Report, NPS-PH-01-001, November, 2000.
26. Colson, W.B., "Tutorial on Classical Free Electron Laser Theory", Nuclear Instruments and Methods in Physics Research, A237 (1985), 109, North Holland, Amsterdam.
27. Fruend, H.P. and Antonsen, T.M., Jr., "Principles of Free-Electron Lasers", Chapman and Hall, London, UK SE1 8HN, 1992.
28. Jackson, J.D., "Classical Electrodynamics", Third Edition, John Wiley and Sons, New York, NY. 1999.
29. Colson, W.B., "Laser Handbook, Vol.6, Chapter 5", Editors W.B. Colson, C. Pellegrini, and A. Renieri, Nor-Holland, Amsterdam. 1990.
30. Massey, D.S., "Simulations of the Darmstadt Free Electron Laser and a Comparison of High Gain Free Electron Lasers." Naval Postgraduate School Masters Thesis, December, 2000.

THIS PAGE INTENTIONALLY LEFT BLANK

INITIAL DISTRIBUTION LIST

- | | | |
|-----|---|---|
| 1. | Defense Technical Information Center
8725 John J. Kingman Rd., STE 0944
Ft. Belvoir, VA 22060-6218 | 2 |
| 2. | Dudley Knox Library
Naval Postgraduate School
441 Dyer Rd.
Monterey, CA 93943-5101 | 2 |
| 3. | Professor William B. Colson, Code PH/Cw
Naval Postgraduate School
Monterey, CA 93943-5117 | 2 |
| 5. | Commander Roger D. McGinnis
5214 Light Street
Springfield, VA 22151 | 2 |
| 6. | Professor Robert L. Armstead, PH/Ar
Department of Physics
Naval Postgraduate School
Monterey, CA 93943-5000 | 1 |
| 10. | Professor James H. Luscombe, PH/Lj
Department of Physics
Naval Postgraduate School
Monterey, CA 93943-5000 | 1 |
| 12. | Professor Andres Larraza, PH/Lz
Department of Physics
Naval Postgraduate School
Monterey, CA 93943-5000 | 1 |
| 13. | Professor David C. Jenn, ECE/Jn
Department of Electrical Engineering
Naval Postgraduate School
Monterey, CA 93943-5000 | 1 |
| 14. | Professor Philip Pace, ECE/Pc
Department of Electrical Engineering
Naval Postgraduate School
Monterey, CA 93943-5000 | 1 |
| 15. | Chairman, Department of Physics
Naval Postgraduate School
Monterey, CA 93940-5000 | 2 |